Materials Horizons

ROYAL SOCIETY OF CHEMISTRY

REVIEW

View Article Online
View Journal | View Issue

Cite this: *Mater. Horiz.*, 2023, **10**, 5457

MXene based flexible photodetectors: progress, challenges, and opportunities

La Li and Guozhen Shen *

Received 28th August 2023,
Accepted 25th September 2023

DOI: 10.1039/d3mh01362f

rsc.li/materials-horizons

The growing interest in applying 2D transition-metal carbides and nitrides (MXenes) to diverse application fields such as energy storage and harvesters, catalysts, sensors, optoelectronics, electromagnetic interference shielding and antennas since its first discovery in 2011 is clearly evident. Their intrinsic high conductivity limits the development of MXenes in photodetectors that rely on the semiconducting properties of active materials, while the abundant functional groups on the surface of MXenes provide opportunities for using MXenes as sensing materials in the fabrication of flexible photodetectors. Considerable studies on MXene based photodetectors have been carried out, but the main obstacles include seeking novel semiconducting materials in MXene families, the manufacturing technology, *etc.* This review highlights the progress, challenges and opportunities in MXene based flexible photodetectors and discusses novel materials, architectures, and approaches that capitalize on our growing understanding of MXenes.

Wider impact

2D transition-metal carbide and nitride (MXenes) based flexible photodetectors have attracted great interest in recent years owing to their high conductivity, superior mechanical stability, and tunable bandgap. Since their first discovery in 2011, more than 40 different compositions have been synthesized by selective etching of the MAX phase and other precursors, and many members from MXene families have theoretically been predicted to have semiconducting properties, offering great application potential in flexible optoelectronic devices. However, we found that there are few review papers discussing MXene applications in flexible optoelectronic fields. In this review, we will summarize the recent research progress of MXene based flexible photodetectors and outline the challenges and opportunities for their further development. This review will help people to understand the current status of MXene based flexible photodetectors, which is of importance for researchers whose scientific interests are focused on flexible optoelectronic devices.

School of Integrated Circuits and Electronics, Beijing Institute of Technology, Beijing 100081, China. E-mail: lali@bit.edu.cn, gzshen@bit.edu.cn

La Li

La Li received her PhD degree in applied physics at Jilin University in 2018. She is currently an associate professor at the School of integrated circuits and electronics, Beijing Institute of Technology, China. Her research interests mainly focus on 2D MXene based flexible optoelectronic devices.

Guozhen Shen

Guozhen Shen received his PhD degree (2003) in Chemistry from University of Science and technology of China. He then conducted research in several countries, including Korea, Japan, US and China. Currently, he is a professor at the School of Integrated Circuits and Electronics and director of Institute of Flexible Electronics, Beijing Institute of Technology. His research focuses on flexible electronics and printable electronics and their applications in healthcare monitoring, smart robots and related areas.

1. Introduction

2D transition-metal carbides and nitrides (MXenes) produced by selective exfoliation of MAX phases (A is a main group sp element from groups 13 and 14) correspond to the general formula $M_{n+1}X_nT_x$, where M is an early transition metal, X represents carbon and/or nitrogen, T_x stands for hydroxyl (–OH), oxygen (–O), or fluorine (–F) termination, n = 1–4.[1–4] In addition to their sharp excellence in the field of energy storage,[5–9] sensors,[10–16] triboelectric devices,[17] electromagnetic interference shielding,[18–20] transparent electrodes,[21,22] catalysis,[23] thermoelectric,[24] water purification,[25] and desalination since their first synthesis in 2011,[26–28] the application of MXenes in various flexible optoelectronic devices that cannot be ignored has aroused increasing attention triggered by their outstanding mechanical, physical and chemical properties.[29–33]

The reasons why MXenes are regarded as a promising material for flexible optoelectronic devices are as follows: (1) the ultra-thin thickness of about 1 nm promotes the strong van der Waals junction with other 2D nanosheets.[34–37] Xu *et al.* reported MXene electrodes for the tiny connection between 2D WSe_2 single nanoflakes and MoS_2 nanosheets, which show great potential in field effect transistors.[38] (2) Superior flexibility provides natural advantages for flexible electronic devices. Alhabeb and co-workers demonstrated the outstanding mechanical properties of $Ti_3C_2T_x$ MXene films over various deformable substrates *via* different technologies such as vacuum assisted filtration, spray coating, and painting.[39] (3) High conductivity enables an outstanding ohmic contact. The reported highest electrical conductivity reaches up to 2.4 × 10^4 S cm^{-1}.[40] (4) Tunable semiconducting features enable them to work as photosensitive materials of the photodetector. Theoretical studies have predicted that Ti_2CO_2, Zr_2CO_2, Hf_2CO_2, Sc_2CF_2, $Sc_2C(OH)_2$, and Sc_2CO_2 have bandgaps of 0.24 eV, 0.88 eV, 1.0 eV, 1.03 eV, 0.45 eV, and 1.80 eV, respectively, which correspond to the visible light absorption range.[41] (5) Sufficient transparency contributes to building transparent flexible electronic devices. A transmittance of 91.2% is obtained for a 5 nm $Ti_3C_2T_x$ MXene film and a transmittance of 43.8% still remains when the thickness of the film reaches 70 nm.[42] (6) Improved stability facilitates long-term serving photodetectors. Mathis *et al.*[43] demonstrated an environmentally stable Al–$Ti_3C_2T_x$ MXene for more than 10 months.

These excellent features have promoted extensive research on MXene based flexible optoelectronics, and great achievements have been gained in the exploration of novel MXene devices.[44,45] There are many reviews on MXene based flexible optoelectronic devices,[46–49] and as they have summarized the synthesis methods of MXenes, we will not repeat them here. In this review, we systematically summarize the recent progress in MXene based flexible photodetectors, as shown in Fig. 1. We first present a brief overview of recent advances from materials to fabrication technology to devices to applications based on

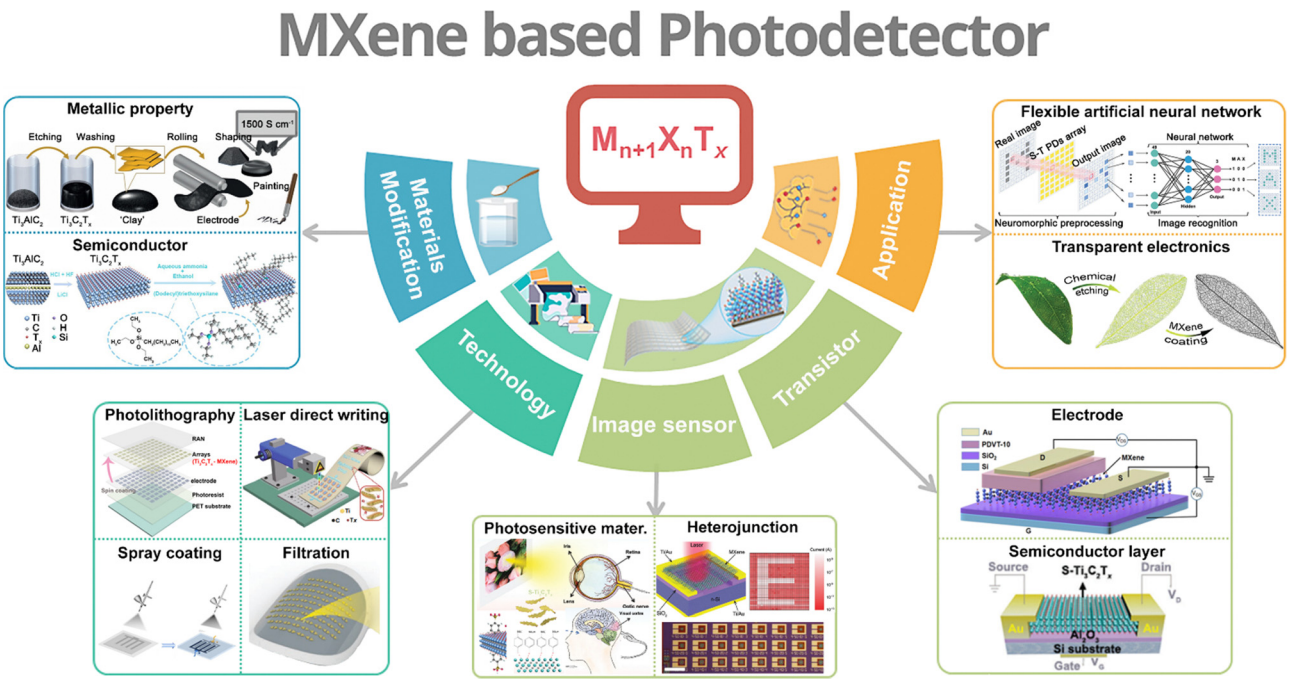

Fig. 1 Overview of MXene based flexible photodetectors. Materials modification: metallic properties.[50] Reproduced with permission. Copyright 2014, Springer Nature. Semiconductor.[51] Reproduced with permission. Copyright 2023, AIP Publishing. Technology: photolithography.[52] Reproduced with permission. Copyright 2022, Wiley-VCH. Laser direct writing.[53] Reproduced with permission. Copyright 2021, Springer. Spray coating.[54] Reproduced with permission. Copyright 2023, Royal Society of Chemistry. Filtration.[55] Reproduced with permission. Copyright 2019, Wiley-VCH. Image sensor: heterojunction.[56] Reproduced with permission. Copyright 2022, Wiley-VCH. Photosensitive materials.[57] Reproduced with permission. Copyright 2023, Wiley-VCH. Transistor: electrode.[58] Reproduced with permission. Copyright 2022, Springer Nature. Semiconductor layer.[57] Reproduced with permission. Copyright 2023, Wiley-VCH. Application: flexible artificial neural network.[57] Reproduced with permission. Copyright 2023, Wiley-VCH. Transparent electronics.[59] Reproduced with permission. Copyright 2020, Royal Society of Chemistry.

MXene materials. Section 2 mainly covers the surface engineering of MXenes, including their intrinsic metallic conductivity and strategies toward semiconductive MXenes.[50,51] And then, fabrication procedures for MXene electronics are introduced, for example, photolithography,[52] laser direct writing,[53] spray coating,[54] filtration,[55] *etc.* In Section 4, we focus on promising optoelectronic devices based on MXenes. Image sensors constructed with photodetector arrays are divided into two groups, one is a heterojunction where various materials are facilitated to engage in Schottky barrier based photodetectors according to the adjustable work function of MXenes.[56] The other refers to using pure semiconducting MXenes as photosensitive materials of photodetector materials.[57] The transistor in this section is also discussed, and both MXene electrodes (source, drain, and gate electrodes)[58] and semiconducting MXene layers are outlined.[57] Then some critical concepts associated with MXene based optoelectronic devices that contain a flexible artificial neural network[57] and transparent electronics[59] are provided. The challenges and perspectives on the development of MXene based optoelectronic devices are outlined in the last part.

2. Surface engineering of MXenes

2.1 Natural metallic properties

The high electrical conductivity is the most attractive feature of MXene materials, which provide possibilities of MXene conductive electrodes in various devices, including supercapacitors, batteries, photodetectors, sensors and transistors.[60–62] In comparison with traditional metal electrodes such as deposited Au, Ti, and Ag conductive film electrodes *via* the vacuum thermal evaporation technique or Pt electrode film electrodes prepared by the magnetron sputtering method, MXene film electrodes applied in the fabrication of functional devices perform more flexing and are adaptable (substrate-free, additive free, *etc.*), and will be discussed in the next subsection. The rise in the electrical conductivity of MXenes goes through for a period of time. At first, the conductivity value is about 8000 S cm^{-1} using both the mixed acid method and the minimally intensive layer delamination (MILD) method. So far, the highest electrical conductivity reported in the literature is 24 000 S cm^{-1}.[40] We summarize a comparatively high electrical conductivity along with the preparation methods to obtain the highly conductive MXene films in Fig. 2.

Recently, Zhang *et al.* proposed a size selection assisted with the blade-coating method to improve the electrical conductivity of $Ti_3C_2T_x$ MXene,[63] as shown in Fig. 2a–d. Small flake size and relatively poor flake alignment of the MXene films prepared by solution-based processing leads to an electrical conductivity decrease. Therefore, the authors performed the size selection from the first synthesis beginning of the MAX phase, and Fig. 2a presents the schematic synthesis procedure of the $Ti_3C_2T_x$ MXene flakes from the selected large Ti_3AlC_2 MAX phase, the average lateral size of which is greater than 10 μm, resulting in the average lateral size of $Ti_3C_2T_x$ MXene flakes reaching up to 10 ± 2.1 μm using a modified minimally intensive layer delamination (MILD) method. Fig. 2b displays the $Ti_3C_2T_x$ MXene film *via* a blade coated technique, which ensures the densified stacking of ordered large MXene flakes (Fig. 2c) and delivers a high conductivity of 15 100 S cm^{-1} with 2.4 μm thick film (Fig. 2d). It's important to notice the $Ti_3C_2T_x$ MXene film was treated under vacuum at 200 °C for 6 h (10 200 S cm^{-1} before treatment). Although the blade-coating technique is difficult to apply in the electrode preparation of flexible optoelectronic devices that possess a micro or nano size, this work provides two common methods containing size selection of the MAX phase and heat treatment of the MXene film to realize the electrical conductivity improvement.

Furthermore, Gogotsi's group[43] demonstrates the increase in electronic conductivity of $Ti_3C_2T_x$ MXene produced by the modified Ti_3AlC_2 MAX phase precursor, in which excess aluminium was added (marked as Al–Ti_3AlC_2). Fig. 2e shows the schematic of Al–Ti_3AlC_2, the excessive Al provides the Ti_3AlC_2 grains with improved crystallinity and carbon stoichiometry. Fig. 2f shows the digital photos of the Al–Ti_3AlC_2 MAX phase. The TEM image of Al–$Ti_3C_2T_x$ MXene synthesized from Al–Ti_3AlC_2 precursor is presented in Fig. 2g. Fig. 2h depicts the electronic conductivity of Al–$Ti_3C_2T_x$ MXene, the freestanding Al–$Ti_3C_2T_x$ MXene film obtained by a vacuum filtering method have conductivities ranging from slightly higher than 10 000 S cm^{-1} up to values exceeding 20 000 S cm^{-1}. More importantly, the Al–$Ti_3C_2T_x$ MXene exhibits long-term stability with no obvious change over 10 months stored under ambient conditions, which is inspiring features for preparing MXene electrodes of flexible optoelectronic devices.

In the same year, Shayesteh *et al.*[40] proposed an evaporated nitrogen MILD (EN-MILD) method to produce $Ti_3C_2T_x$ MXene with increased electrical conductivity. Fig. 2e shows a schematic of the synthesis approach, the reaction contains the MAX phase, and the acid solution was connected to the nitrogen source and a vent. The evaporated nitrogen eliminates dissolved oxygen and increases the acid and Li-ion concentrations, which is beneficial for the etching of the MAX and promotes better dissolution of LiF. Fig. 2j displays the optical image of the obtained $Ti_3C_2T_x$ MXene suspension and the freestanding $Ti_3C_2T_x$ MXene film prepared *via* a vacuum assisted filtration method. The $Ti_3C_2T_x$ MXene film exhibits superior flexibility, as shown in Fig. 2j. The measured electrical conductivity of the $Ti_3C_2T_x$ MXene film exceeds 240 000 S cm^{-1}. This highly conductive $Ti_3C_2T_x$ MXene derived from the modified synthesis approach give ways to prepare other types of MXene materials with high conductivity in the same methods, which can be applied to the fabrication of MXene based optoelectronic devices.

2.2 Strategy toward semiconductors

The semiconducting properties of MXene materials are the main precondition that decides whether they can be used in the fabrication of flexible optoelectrical devices as active materials instead of conductive electrodes. To date, about 150 MAX phases have been reported, and more than 40 MXenes have been synthesized.[64,65] Among them, some MXenes have been predicted as intrinsic semiconductors according to the computational theoretical study. Besides, the surface terminals also affect

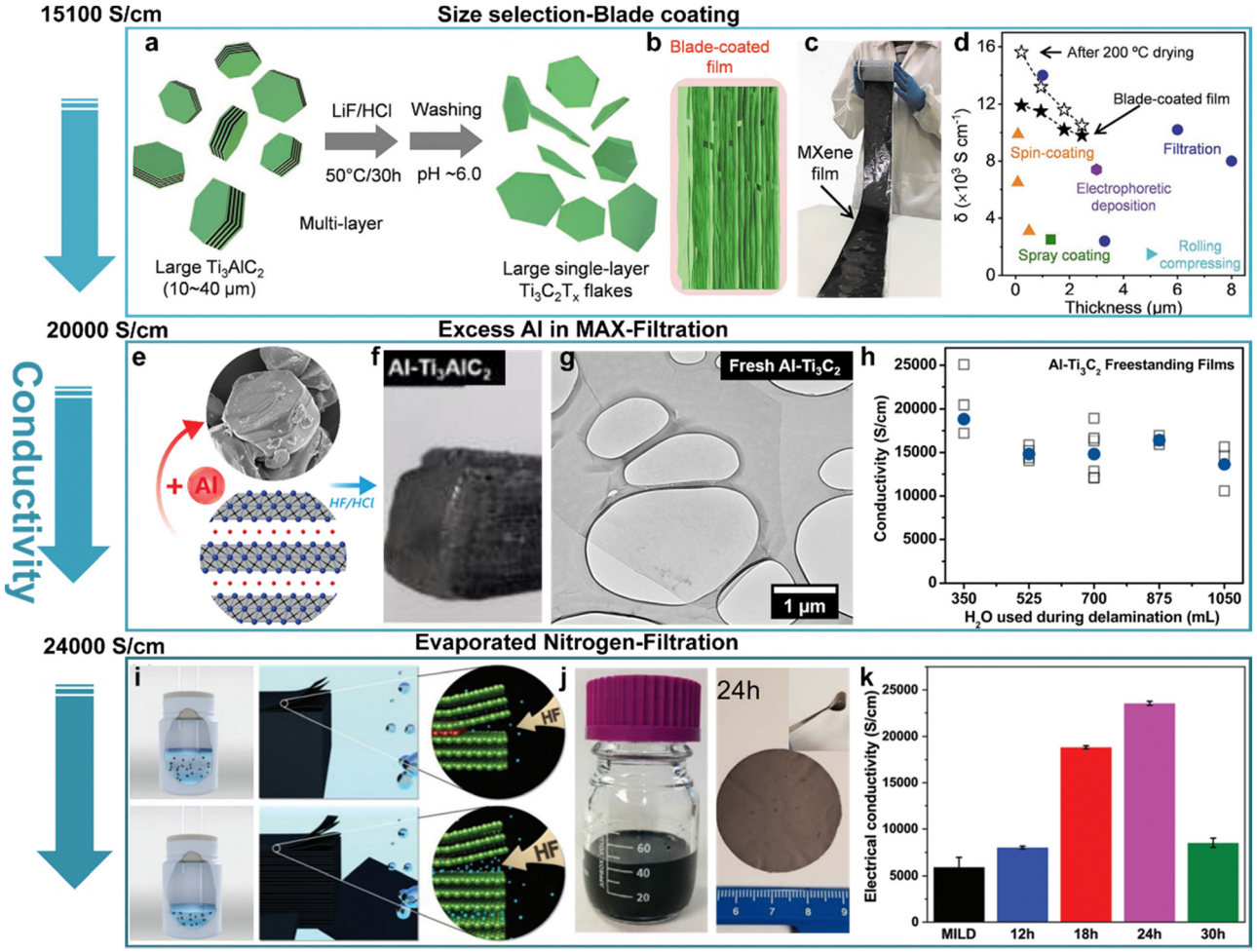

Fig. 2 The rising electrical conductivity of $Ti_3C_2T_x$ MXene films. (a)–(d) Improved electrical conductivity of $Ti_3C_2T_x$ MXene by size selection of the MAX phase and blade coating technology.[63] Reproduced with permission. Copyright 2020, Wiley-VCH. (e)–(h) Increased electrical conductivity of $Ti_3C_2T_x$ MXene *via* excess Al in the synthesis of the MAX phase.[43] Reproduced with permission. Copyright 2021, American Chemical Society. (i)–(k) Increased electrical conductivity of $Ti_3C_2T_x$ MXene through evaporated nitrogen minimally intensive layer delamination (EN-MILD) methods.[40] Reproduced with permission. Copyright 2021, Royal Society of Chemistry.

the work function of the MXenes.[66,67] For example, the 2D single-layer Ti_2CO_2, Zr_2CO_2, Hf_2CO_2, Sc_2CF_2, $Sc_2C(OH)_2$, and Sc_2CO_2 are calculated with band gaps of 0.24 eV, 0.88 eV, 1.0 eV, 1.03 eV, 0.45 eV, and 1.80 eV, respectively, by using the PBE functional computations, providing the feasibility of MXenes as photo-sensitive materials in the flexible photodetector.[68] Fig. 3 gives a summary of the semiconductor properties demonstration history of MXenes, from theory study to *in situ* TEM observation, and finally constructing the MXene-sensitive semiconductor device.

The theoretical studies of MXenes (M_2CT_2, M = Ti, Zr, Hf; T = O, F, OH)[41] are presented in Fig. 3a–c. Fig. 3a shows the geometries of the Ti_2C and Ti_2CO_2 MXene. The M_2CT_2 MXene materials were functionalized by the surface groups of –O, –F and –OH. In this work, the authors marked three groups M_2CT_2-I, M_2CT_2-II, and M_2CT_2-III, where both sides of the surface groups were located above the opposite-side metal atoms (M_2CT_2-I), mid-layer carbon atoms, (M_2CT_2-II). M_2CT_2-III has a one side functional group located above the opposite metal atoms, while the other side functional group is located above the mid-layer carbon atoms. Fig. 3b shows the electron localization functions of the M_2CO_2-I. According to their calculation results, the favorable M_2CO_2-I have suitable band gaps (0.92–1.75 eV). The band edge position of Ti_2CO_2, Zr_2CO_2, and Hf_2CO_2 in Fig. 3c reveals the Ti_2CO_2-I, Zr_2CO_2-I, and Hf_2CO_2-I have band gaps of 0.92, 1.54, and 1.75 eV, respectively. This work gives us the theoretical foundation for the use of MXene materials in optoelectric devices.

In 2019, Gogotsi's group[69] demonstrated the transitions of MXenes between metallic and semiconductor-like transport through inter-flake effects *via in situ* vacuum annealing within the transmission electron microscope (TEM), as shown in Fig. 3d–f. Fig. 3d depicts the nanochip for TEM analysis. Different MXenes were spray coated on the nanochip, which was heated under a vacuum. The properties change with different MXenes and different intercalators are provided in Fig. 3e. $Ti_3C_2T_x$ MXene exhibits metallic behavior as the temperature increases. While Ti_3CNT_x and $Mo_2TiC_2T_x$ display semiconductor-like behavior. Obviously, the intercalators used in the delamination process of the MXenes also have effects on their properties. In detail, Ti_3CNT_x MXene

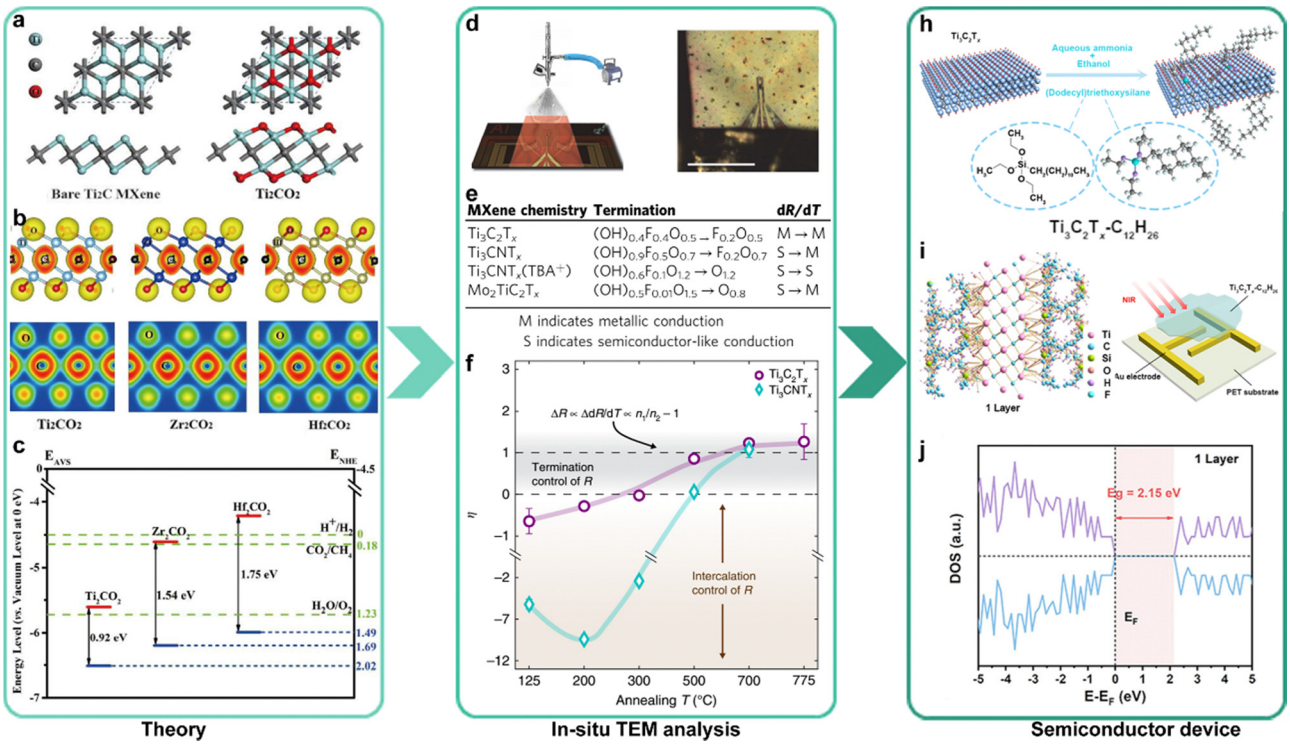

Fig. 3 The semiconductor properties demonstration of MXenes. Computational study.[41] (a) Geometries of the Ti_2C and Ti_2CO_2 MXene. (b) The electron localization functions of the Ti_2CO_2, Zr_2CO_2, and Hf_2CO_2. (c) The band edge position. Reproduced with permission. Copyright 2016, Royal Society of Chemistry. Evolution of MXene electronic properties with *in situ* vacuum annealing.[69] (d) Nanochip for TEM analysis. (e) The properties change with different MXenes and different intercalators. (f) The resistance changes during the annealing process. Reproduced with permission. Copyright 2019, Springer Nature. MXene materials applied in the semiconductor device.[51] (h) Preparation of $Ti_3C_2T_x$–$C_{12}H_{26}$ MXene. (i) and (j) Band gap calculations for $Ti_3C_2T_x$–$C_{12}H_{26}$ MXene with different layers. Reproduced with permission. Copyright 2023, AIP Publishing.

intercalated by LiCl shows a transition of MXenes from semiconductor-like to metallic transport, once the intercalator is changed with TBAOH, the Ti_3CNT_x MXene exhibit constant semiconductor-like transport. The resistance changes of MXenes during vacuum treatment at temperatures up to 775 °C are displayed in Fig. 3f. The semiconductor-like (negative dR/dT) behavior of the Ti_3CNT_x MXene can be clearly seen, which provides strong evidence for the inherent semiconductor MXenes.

Recently, our research group demonstrated the $Ti_3C_2T_x$ MXene modified with dodecyl ($-C_{12}H_{26}$) groups possess an opened and tunable bandgap by controlling the thickness of the functional $Ti_3C_2T_x$–$C_{12}H_{26}$ MXene materials, which further served as photosensitive materials of a flexible photodetector.[51] Fig. 3h shows the schematic preparation process of $Ti_3C_2T_x$ modified with dodecyl ($-C_{12}H_{26}$). Owing to the abundant functional groups on the surface of $Ti_3C_2T_x$, the molecules of (dodecyl) triethoxysiloxane DCTES hydrolyzed into unstable silanols and covalently bonded with hydroxyl groups on the surface of $Ti_3C_2T_x$ to complete the grafting of $-C_{12}H_{26}$ and form $Ti_3C_2T_x$–$C_{12}H_{26}$ MXene. The $Ti_3C_2T_x$–$C_{12}H_{26}$ MXene exhibits a layer-dependent band gap after Raman analysis and DFT calculations, as shown in Fig. 3i and j. In addition, the photoluminescence (PL) spectrum, together with photoelectric measurements of $Ti_3C_2T_x$–$C_{12}H_{26}$ MXene on the different layers show a tunable bandgap of 0.49–2.15 eV and superior photoresponse properties in fabricating near infrared photodetectors.

3. Fabrication procedure

A suitable technology is important for fabricating flexible optoelectric devices. In this section, we will introduce the reported manufacturing technology in the preparation of flexible photodetectors. The photolithography method is the most comment method used in micro-nano scale devices. A laser direct writing technique with the advantage of being mask-free also becomes the necessary manufacturing technology to fabricate photodetector devices. Then spray coating and filtration method routing from the specialties of MXene materials are presented at the end of this section.

3.1 Photolithograph

Photolithography as a well-developed technology has been widely employed in preparing insulated or conductive layers according to the preset pattern with high resolution and minimal size, which is suitable for fabricating micro-nano scale photodetectors devices.[70,71] Fig. 4a shows the schematic illustration of the structures of a flexible photodetector with Mxene electrodes *via* the photolithography process.[52] In a typical procedure, the flexible PET substrate was placed in plasma cleaner for 30 min to enhance the hydrophilicity and wettability. Then, the photoresist was spread on the PET substrate. Subsequently, a conventional photolithographic process was carried out. Next, the $Ti_3C_2T_x$ Mxene was spin-coated. Finally, after removing the photoresist, photosensitive

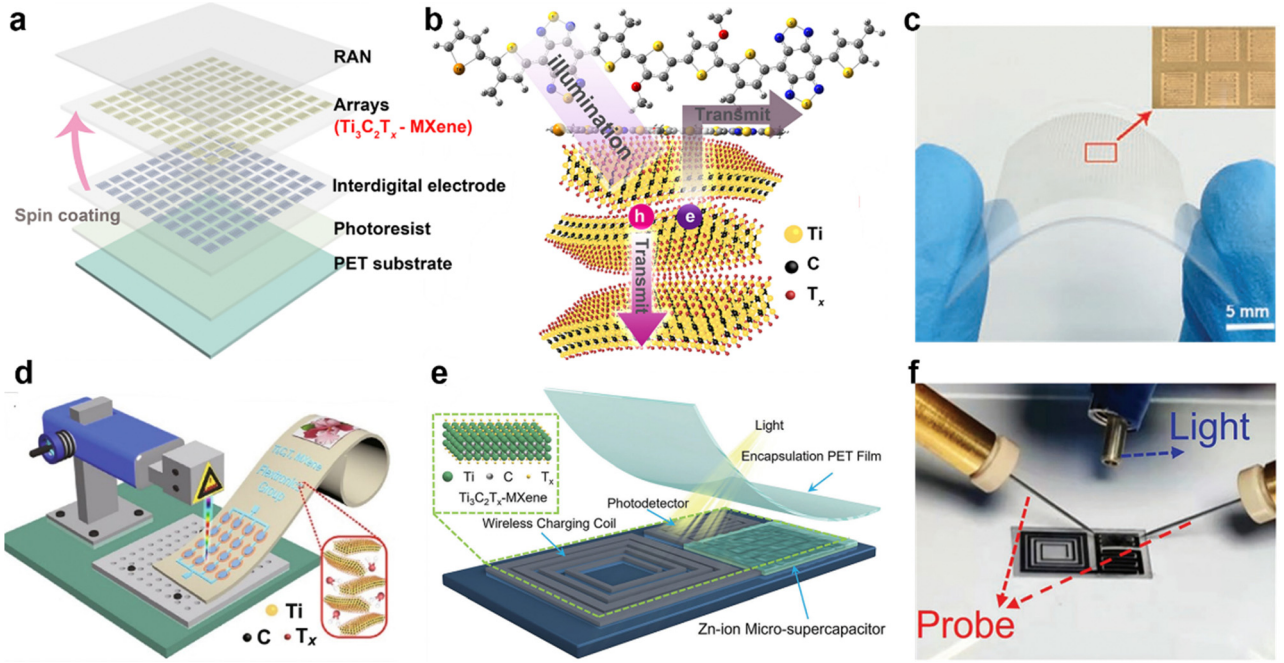

Fig. 4 Device Fabrication Technology. Photolithography.[52] (a) Schematic illustration of the photolithography process for fabricating the flexible photodetector. (b) The electronic transmission of the $Ti_3C_2T_x$–RAN based active materials. (c) The digital photos of the fabricated photodetector arrays *via* photolithography method. Reproduced with permission. Copyright 2022, Wiley-VCH. Laser direct writing. (d) Schematic of the laser direct writing procedure for fabricating the MXene based flexible photodetector.[53] Reproduced with permission. Copyright 2021, Springer. (e) The structures of the fabricated multifunctional devices. (f) The photograph of the devices for testing the photodetection performance.[72] Reproduced with permission. Copyright 2023, Wiley-VCH.

RAN materials were spread on the integrated $Ti_3C_2T_x$ Mxene electrode array. The fabricated $Ti_3C_2T_x$–RAN based photodetector exhibits a stable photo response under laser illumination, the properties will be discussed in detail in the next subsection. It can be seen that the fabricated flexible photodetector with a $Ti_3C_2T_x$ MXene electrode array following this process keeps the high resolution and large-scale array of the photolithography. Moreover, the $Ti_3C_2T_x$ MXene electrode array shows three superiorities: (1) an all-room temperature manufacturing process. Unlike conventional metal electrodes such as Au, Ag, and Pt electrodes that rely on vacuum and high temperature atmospheres supplied by the thermal evaporation and magnetron sputtering equipment. (2) From a Schottky junction with $Ti_3C_2T_x$, which reduces the barrier height and increases the conductivity of the channel (Fig. 4b). (3) High transparency and flexibility (Fig. 4c), over 70% transmittance in the visible region and no obvious performance degradation under the bending state suggest the high transparency and mechanical stability of the $Ti_3C_2T_x$ MXene electrode based photodetector.

3.2 Laser direct writing

The laser direct writing method with features of universal adaptability, facility, variable-area patterns, high resolution, high throughput, and optimal control of feature size, has been induced in the fabrication of flexible photodetectors.[73] This technique has no need for active materials. Fig. 4d shows the typical schematic of the laser direct writing procedure for fabricating micro-nano devices.[53] Our group reported on an all $Ti_3C_2T_x$ MXene based flexible, seamless system (Fig. 4e), and it's worth noting that the integrated wireless charging coil, micro-supercapacitor, and photodetector were all prepared *via* the laser direct writing approach.[72] Fig. 4f displays the photograph of the devices for testing the photodetection performance. The $Ti_3C_2T_x$ electrode was cut by the laser according to the pre-designed pattern with different functions. The $Ti_3C_2T_x$ MXene based functional devices prepared by the laser direct writing method have the advantages of an all-room temperature manufacturing process and one-step for multifunctional devices, which is necessary for future integrated electronic devices. Moreover, the laser direct writing method is considered a promising technology due to its ability to realize large-area manufacturing of micro-nano devices.

3.3 Spray coating

The spray coating techniques are simple and cost-effective ways to fabricate patterned films, especially, to prepare the $Ti_3C_2T_x$ MXene film because of its high concentration in water-based solvent and excellent hydrophilic properties. Our group proposed a self-powered flexible photodetector using $Ti_3C_2T_x$ MXene materials *via* the spray coating method,[54] as shown in Fig. 5a. From the schematic diagram of the fabrication process, we can see the $Ti_3C_2T_x$ MXene conductive electrode was sprayed vertically through the mask plate on the flexible PET substrate, which was heated at 80 °C. The thickness of the $Ti_3C_2T_x$ MXene film can be adjusted by the distance between the mask plate and the spray gun. It is emphasized that the mask plate and the

substrate must be in close contact to prevent the occurrence of short circuits. Fig. 5b illustrates the digital photos of the fabricated devices under testing. Different from the photolithographic technique and laser direct writing method, spray coating techniques could be scalable for fast and low-cost production and offer complex planar geometries on various flexible substrates, paving a new technical route for large-scale fabrication of MXene based flexible integrated electronic devices.

3.4 Filtration

The vacuum filtering (vacuum assisted filtration) method is a promising way for preparing free standing $Ti_3C_2T_x$ MXene films with different thicknesses and diverse planar geometries. Fig. 5c depicts a schematic of the vacuum assisted filtration procedure.[74] Recently, Velusamy *et al.*[55] developed a Mo_2CT_x MXene based flexible photodetector by employing a vacuum assisted filtration technique. In detail, the homogeneous Mo_2CT_x MXene thin films ($\approx$2 μm thick) were deposited on nylon membranes (filter papers) *via* vacuum-assisted filtration from Mo_2CT_x MXene suspensions. Then, 50 nm thick conductive Au electrodes were deposited on the prepared Mo_2CT_x MXene thin films *via* e-beam evaporation, giving rise to mechanically flexible arrays of two-terminal, parallel-type devices with a channel length and width of 70 μm and 1 mm, respectively. Fig. 5d shows the schematic illustration of an array of Mo_2CT_x based flexible photodetectors. The corresponding digital photograph of the fabricated device arrays is provided in Fig. 5e, which demonstrates that vacuum filtering was also performed to show the potential of scale-up production of microelectronic devices and opens a new avenue to scalable fabrication of high-performance flexible optoelectronic devices.

4. Optoelectronic devices

4.1 Image sensor

Image sensors constructed by photodetector arrays have broad application prospects in biomedicine, accurate image sensing, visual simulation, and human vision recovery and treatment owing to their advantages of portability and wearability and can display a high-resolution picture to enhance imaging ability.[75–79] MXenes with ultra-thin thickness and deserving functional groups have gained extensive attention for fabricating flexible photodetectors in recent years. In this section, various MXenes heterojunction and pure MXene based photodetectors, along with the corresponding detection mechanisms will be given.

4.1.1 Heterojunction. Recently, Barsoum's group[80] reported on GaAs based photodetectors by making transparent $Ti_3C_2T_x$ MXene electrodes on the ends of GaAs materials (MX–S–MX) patterned with photolithography technology. Standard Au electrodes were also fabricated in contrast. The energy band diagram of the MX–S–MX devices under high biasing voltage shows the formation of Schottky barriers, built-in potential and depletion regions. In comparison with the traditional Au electrode, the MX–S–MX photodetector possesses metal–semiconductor–metal (M–S–M) junctions. The similar I_{dark} along with the remarkable five orders of magnitude change in photocurrent demonstrate that MXene is as good as Ti/Au electrodes, providing an excellent choice for photoelectrical devices. Our group[52] also demonstrates a $Ti_3C_2T_x$ MXene–RAN van der Waals heterostructure-based flexible transparent near photodetector with a higher on–off ratio (6.25 times higher) compared with an Au–RAN photodetector.

Except for replacing Au electrodes with $Ti_3C_2T_x$ MXene electrodes, the $Ti_3C_2T_x$ MXene could form a heterojunction with conventional metal-oxide semiconductors; such as zinc

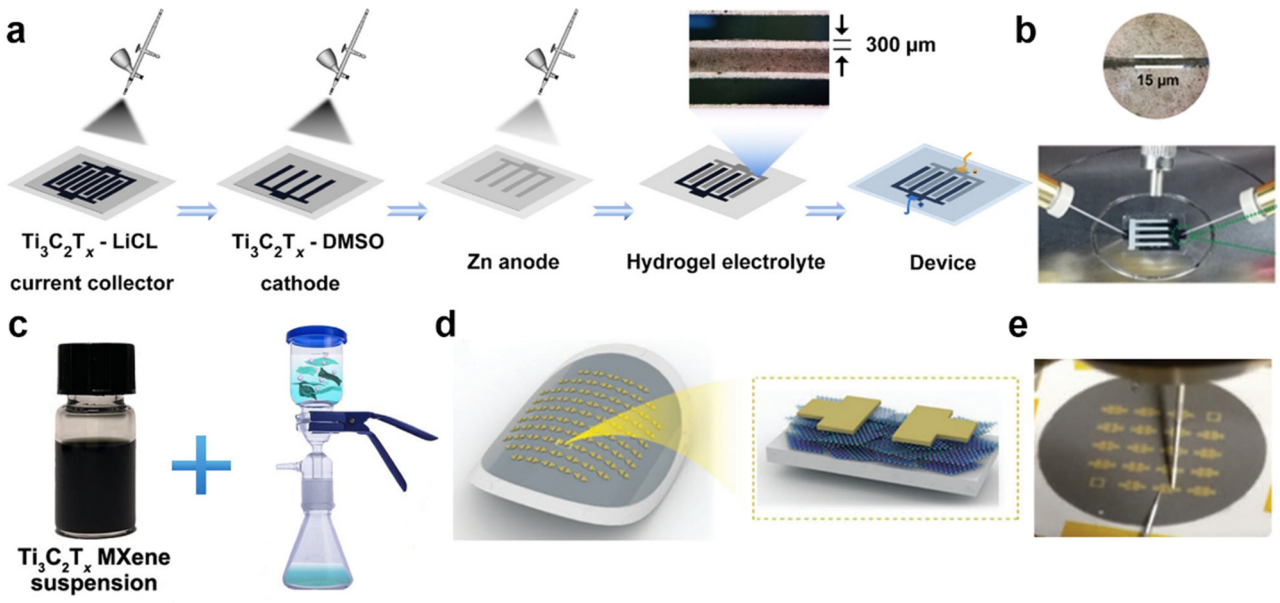

Fig. 5 Device Fabrication Technology. Spray coating.[54] (a) Schematic illustration of the spray coating process for fabricating the flexible self-powered photodetector. (b) The digital photos of the fabricated devices. Reproduced with permission. Copyright 2023, Royal Society of Chemistry. Filtration. (c) Schematic of the vacuum assisted filtration procedure.[74] Reproduced with permission. Copyright 2022, Wiley-VCH. (d) The schematic illustration of an array of Mo_2CT_x based flexible photodetectors. (e) The photograph of the devices.[55] Reproduced with permission. Copyright 2019, Wiley-VCH.

oxide, titanium oxide, and tin oxide.[81–84] It is well known that single Ti-based MXene flakes in the colloidal state can possibly be spontaneously oxidized at oxygen content in the environment, leading to the *in situ* formation of MXene/TiO_2 composites.[85] Inspired by the spontaneous oxidation phenomenon, Chertopalov and co-workers[86] studied the photoresponse performances of partially oxidized $Ti_3C_2T_x$ MXene thin films. Fig. 6a shows the schematic diagram of an *in situ* partially oxidized $Ti_3C_2T_x/TiO_2$ photodetector. The single $Ti_3C_2T_x$ flakes were obtained through MILD methods and delaminated by a handshaking process, which were then deposited on the glass substrate and exposed to air for partial oxidation. The $Ti_3C_2T_x/TiO_2$ heterostructure based thin film on a glass substrate is displayed in Fig. 6b, the cross section of the film depicts TiO_2 nanoparticles located between and on the surface of the MXene flakes. The spectral region of the hybrid film corresponding to the UV range can be explained by the presence of TiO_2 in air-exposed $Ti_3C_2T_x$ films. Then the electrical properties were investigated, the linear IV curves (Fig. 6c) of a $Ti_3C_2T_x/TiO_2$ thin film of 16 nm with and without UV irradiation in Ar atmosphere suggested the ohmic contacts in the $Ti_3C_2T_x/TiO_2$ thin film. The on–off ratio of the $Ti_3C_2T_x/TiO_2$ based photodetector was calculated to be 1.5 at 1 V DC. The Nyquist plots of $Ti_3C_2T_x/TiO_2$ films applied with 1 V bias and 20 mV in Fig. 6d reveal the thin film impedance is composed of real and imaginary parts. The capacitance/resistance of the $Ti_3C_2T_x/TiO_2$ is about 18 pF/134 Kohm and 22 pF/86 Kohm assigned to UV illumination off and on, respectively, showing an opposite changing tendency in resistance and capacitance with or without UV illumination. To further investigate optoelectronic properties, the authors carried out the cycling photoresponse tests of $Ti_3C_2T_x/TiO_2$ thin film with a thickness of 38 nm under periodic UV irradiation in Ar gas. It was found that the response time is over 20 min while the recovery time is over 2 h (Fig. 6e). Moreover, the photoresponse tests of $Ti_3C_2T_x$/

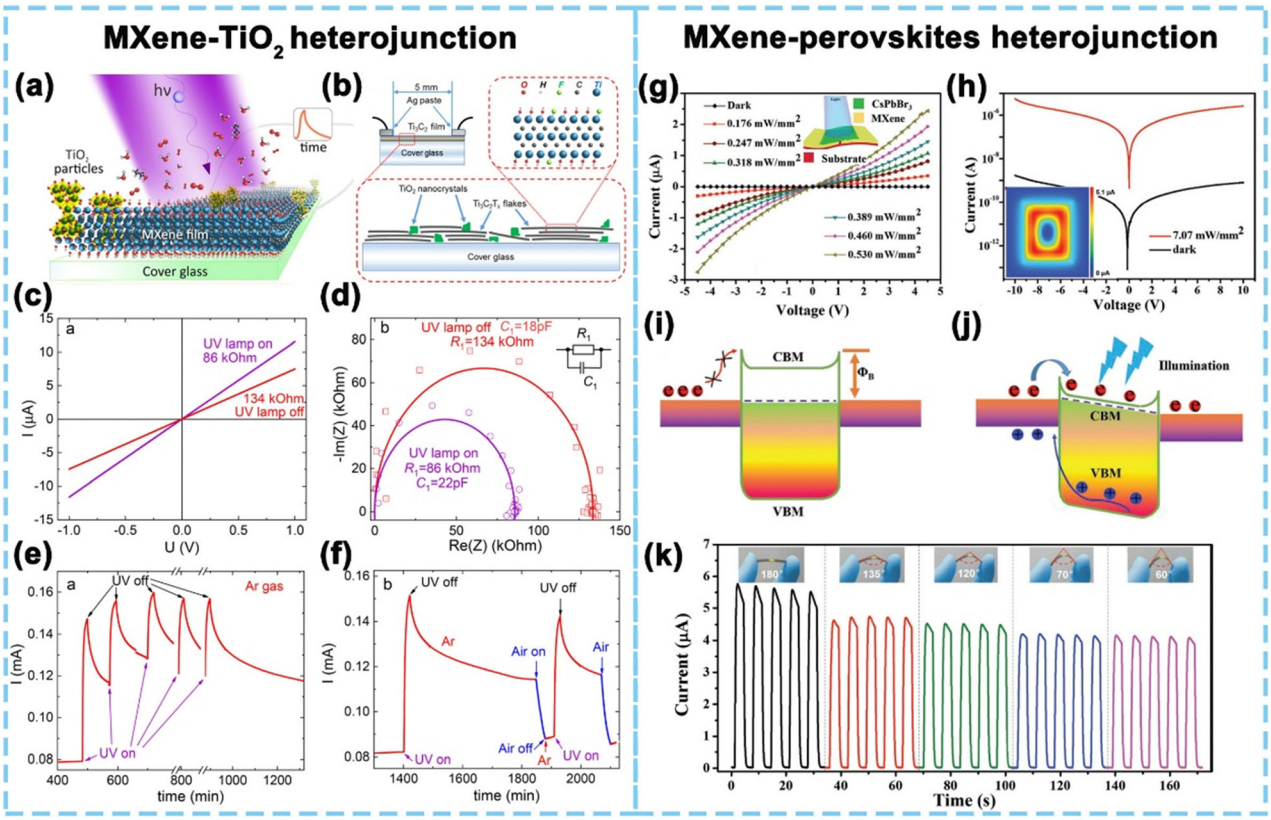

Fig. 6 Divers MXenes heterostructure based photodetector. (a) Schematic diagram of *in situ* partially oxidized Ti_3C_2 MXene photodetectors. (b) Schematics of the $Ti_3C_2T_x/TiO_2$ heterostructure based thin film on cover glass with silver paint contacts, enlarged cross section showing TiO_2 nanoparticles (green) between and on the surface of the MXene flakes. (c) IV curves of a $Ti_3C_2T_x/TiO_2$ thin film of 16 nm with and without UV irradiation under an Ar atmosphere. (d) The corresponding Nyquist plots of $Ti_3C_2T_x/TiO_2$ thin film with (violet circles) and without (red squares) UV irradiation under an Ar atmosphere at a bias potential of 1 V and sinusoidal amplitude of 20 mV. (e) Cycling photoresponse of the $Ti_3C_2T_x/TiO_2$ thin film with a thickness of 38 nm under periodic UV irradiation in Ar gas. (f) Photoresponse of $Ti_3C_2T_x/TiO_2$ thin film under UV irradiation and exposure to ambient air for 30 min.[86] Reproduced with permission. Copyright 2018, American Chemical Society. (g) *I–V* curves of the $Ti_3C_2T_x/CsPbBr_3$ photodetector in the dark and under illumination with 405 nm light at a different intensity from 0.176 to 0.53 mW mm^{-2}. The inset shows a schematic diagram of the fabricated photodetector. (h) *I–V* curves of the single photodetector under light illumination and in the dark. The inset shows the schematic diagram of the fabricated photodetector. The inset is the photocurrent mapping display according to patterned light. (i and j) Schematic diagram of the device's energy level with and without illumination. (k) Flexibility and stability measurement of the as-fabricated $Ti_3C_2T_x/CsPbBr_3$ photodetector.[87] Reproduced with permission. Copyright 2019, Wiley-VCH.

TiO_2 thin film with different thickness demonstrate the response time and the recovery time decrease as the thickness of the MXene film reduces. When the gas was switched from Ar to ambient air (Fig. 6f), the response time significantly decreased. These experiments demonstrate that the photoresponse of the partially oxidized $Ti_3C_2T_x$ MXene thin films is strongly affected by the environment. Although the $Ti_3C_2T_x/TiO_2$ thin film based UV detector shows a controllable photoresponse through changing environmental gas types, the fabricated UV detector undergoes a really poor performance, therefore, more efforts should be dedicated to developing high-performance MXene based photodetectors.

Research on improving the photoresponse properties of MXene based photodetectors has gained increasing interest.[88,89] In a pioneering work, Ouyang *et al.*[90] introduced a $Ti_3C_2T_x$ MXene conduction layer at the interface of a ZnO decorated BiOCl and polydimethylsiloxane (PDMS) based UV photodetector, and the optimized photodetector presents an enhanced photodetecting performance with a responsivity of 2.05 μA W^{-1}, a high on–off ratio of 7996.5, a rapid response/recovery time of 2.59 s/0.93 s and detectivity of 5.86×10^{10} Jones owing to the heterojunction formed between the ZnO NPs and BiOCl nanosheet array and the efficient carrier pathways provided by the $Ti_3C_2T_x$ MXene conduction layers. Very recently, Yang's group[87] reported a flexible high-performance Vis photodetector based on a 2D perovskite $Ti_3C_2T_x/CsPbBr_3$ heterostructure. $Ti_3C_2T_x$ was synthesized using a MILD method and intercalated by handshaking. The inset of Fig. 6g shows the schematic diagram of the fabricated photodetector. *I–V* curves (Fig. 6g) of the $Ti_3C_2T_x/CsPbBr_3$ photodetector in the dark and under illumination with 405 nm light at a different intensity from 0.176 to 0.53 mW mm^{-2} show the photocurrent gradually increases with the enhancement of light intensity. The nonlinear and asymmetrical curves reveal the formation of Schottky contact between MXene and perovskite. In Fig. 6h, *I–V* curves of the single photodetector under 450 nm illumination with 7.07 mW mm^{-2} and dark exhibit a high on/off ratio of 2.3×10^3 under the voltage bias of 10 V. Based on this, superior-quality and large-area 1665-pixel detectors in 72 cm^2 ($\approx$24 units per cm^2) are developed, and they can transmit the image of "0" to realize the photo communication function, as displayed in the inset of Fig. 6h. The transfer mechanism of electron–hole pairs in the $Ti_3C_2T_x/CsPbBr_3$ photodetector is displayed in Fig. 6i and j. The energy level potential barrier (Schottky barrier) of the as-prepared photodetector under dark traps the electrons in the material and cannot allow them to be transported effectively. Once the illumination energy is larger than that of the semiconductor bandgap E_g, the photogenerated electron–hole pairs in $CsPbBr_3$ nanosheets are separated rapidly and can reduce the recombination in these regions increasing the free carrier concentration. The *I–T* curves of the MXene-based PDs at various bending curvatures are exhibited in Fig. 6k, showing excellent flexibility and stability.

Very recently, Kang *et al.*[91] reported MXene–Silicon van der Waals heterostructures for self-driven photodetectors. The stronger photovoltaic effect resulting from the Schottky junction of the as-prepared photodetector between $Ti_3C_2T_x$ MXene and n-type silicon (n-Si) is beneficial to self-powered photodetectors. The work function of $Ti_3C_2T_x$ and n-Si is about 4.35 eV and 3.71 eV, respectively, forming a built-in potential of 0.64 eV, which could promote electron–hole separation and diode-like rectifying behavior. When the heterostructure is exposed to light, photogenerated carriers from n-Si within and near its depletion region should be separated by the built-in electric field and then recombined by the external circuit to generate electrical signals. It's found the on–off ratio can reach up to 10^5 at the zero bias, demonstrating that the fabricated $Ti_3C_2T_x$/n-Si heterostructure device can be used as a good self-powered photodetector. The response and recovery times of the $Ti_3C_2T_x$/n-Si self-driven device are 0.84 ms and 1.67 ms, showing a high-speed response.

4.1.2 Photosensitive materials. On the basis of first-principles calculations, the work function of MXenes can be changed in a wide range by tailoring the surface functional group, which depends on the etching method and delamination process. By comparing the work function of ordinary MXenes and MXenes with a bare surface, it's found that –OH termination has lower work functions between 1.6 and 2.8 eV than that of –O terminated (5.75 and 6.25 eV), while F is strongly affected by the specific material, suggesting the feasibility of MXenes as photosensitive materials in the photodetector.[92,93] The detecting spectral range of a pure $Ti_3C_2T_x$ MXene based photodetector could be broadened through modification of surface terminations, and adjustment of MXene film thickness. These two strategies are often applied together to improve the photoresponse properties and widen the spectral range.

Recently, our group successfully synthesized the phenylsulfonic acid modified $Ti_3C_2T_x$ (S-$Ti_3C_2T_x$) with an opened band gap of 1.53 eV, which was further used as photosensitive materials for fabricating flexible photodetectors.[57] Fig. 7a shows the schematic diagram of the modified S-$Ti_3C_2T_x$ nanosheets. The acid groups dissociate hydrogen ions and form hydrogen bonds with water molecules, resulting in better water dispersibility compared to the unmodified $Ti_3C_2T_x$ MXene. The fabricated device array exhibits excellent mechanical stability with no obvious photocurrent changes under different bending states, as shown in Fig. 7b. Besides, the S-$Ti_3C_2T_x$ photodetector shows a superior photoresponse to near infrared light with the wavelengths of 808–1122 nm. A high responsivity of 8.50×10^2 A W^{-1} and detectivity of 3.69×10^{11} Jones were obtained under 1064 nm light irradiation. A 7×28 (196 pixels) photodetectors array was also fabricated to image the word "MXene" (Fig. 7c), the statistical distribution of photocurrent and dark current of each pixel proved the high performance of the fabricated S-$Ti_3C_2T_x$ image sensor. The mechanical stability of the S-$Ti_3C_2T_x$ image sensor was also measured, and the lack of change in the photocurrent and dark current under different bending states and thousands of bending-release cycles demonstrate the superior flexibility, which can be applied in wearable integrated electronics.

Furthermore, our group also demonstrated the $Ti_3C_2T_x$ MXene possesses a layer dependent band gap,[51] as shown in Fig. 7d–f. Fig. 7d depicts the schematic of the $Ti_3C_2T_x$ MXene modified with dodecyl ($-C_{12}H_{26}$) groups, the new arising characteristics, red-shift of characteristic peaks and intensity ratio

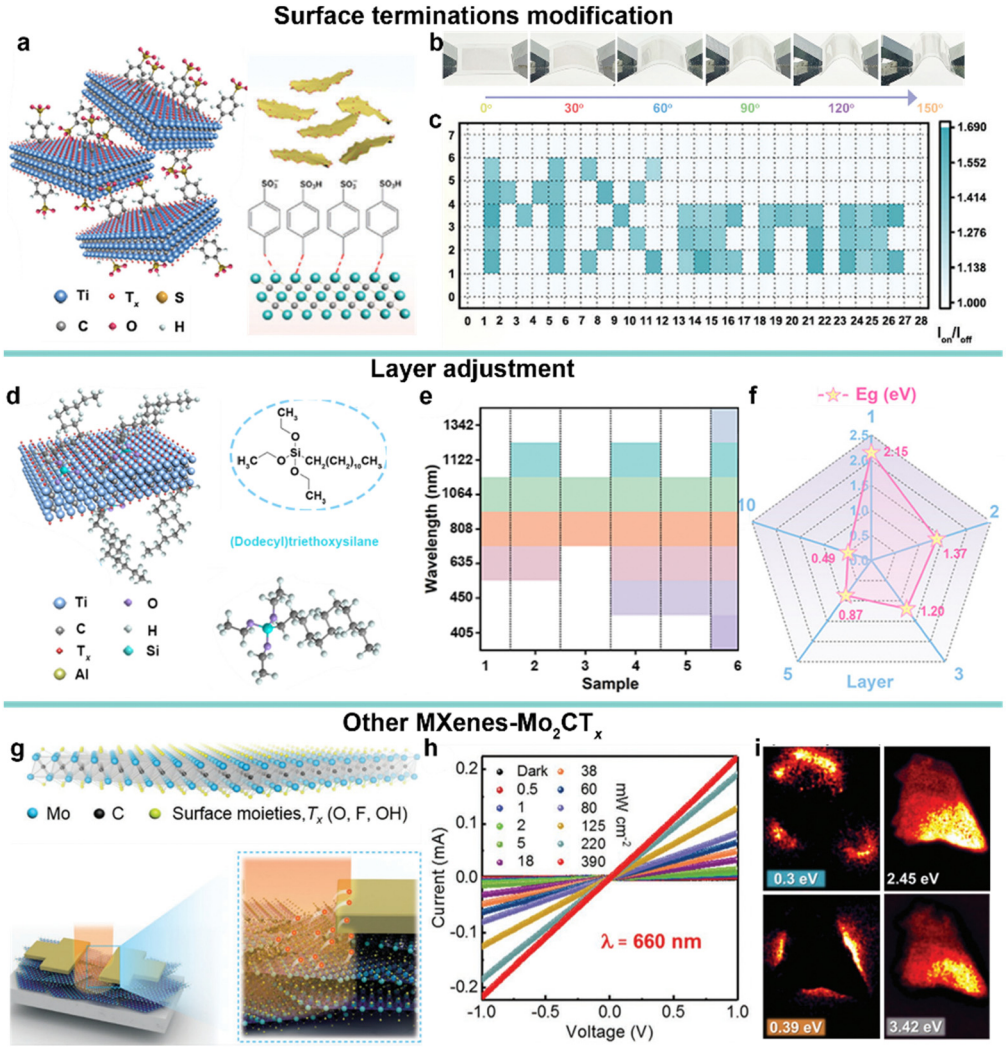

Fig. 7 Pure MXene based flexible photodetector. Surface termination modification.[57] (a) Schematic diagram of the modified $Ti_3C_2T_x$ flakes (S-$Ti_3C_2T_x$). (b) Photographs of the fabricated S-$Ti_3C_2T_x$ devices under different bending states. (c) Multi-pixel points imaging based on S-$Ti_3C_2T_x$ photodetector arrays. Reproduced with permission. Copyright 2023, Wiley-VCH. Layer adjustment.[51] (d) Schematic diagram of the $Ti_3C_2T_x$–$C_{12}H_{26}$. (e) Laser response range diagram of the photodetector with an increased $Ti_3C_2T_x$–$C_{12}H_{26}$ layer. (f) The pattern of the bandgap variation with the number of layer changes. Reproduced with permission. Copyright 2023, AIP Publishing. Other Mxenes–Mo_2CT_x.[55] (g) Schematic illustration of a the Mo_2CT_x nanosheet. (h) The photoresponse of the Mo_2CT_x photodetector under 660 nm illumination. (i) Annular dark field (ADF) STEM micrograph of the Mo_2CT_x nanosheet. Reproduced with permission. Copyright 2019, Wiley-VCH.

of the A_{1g}(C)/A_{1g}(Ti, C, T_x) in Raman spectroscopy suggested the successful grafting of the –$C_{12}H_{26}$ groups on the $Ti_3C_2T_x$ MXenes. Comparing the photoresponse properties of the $Ti_3C_2T_x$–$C_{12}H_{26}$ photodetector with different thickness, it can be seen that all the photodetectors show good optical responses to a 1064 nm laser, and the *I*–*T* curve of PD (about 9 layers) has excellent photocurrent and dark current stability. The device with layers of $Ti_3C_2T_x$–$C_{12}H_{26}$ can be excited by a laser of 405–1342 nm. In addition, $Ti_3C_2T_x$–$C_{12}H_{26}$ MXene with different layers shows a tunable bandgap of 0.49–2.15 eV (Fig. 7f), suggesting the semiconducting properties of the MXene materials with a layer-dependent band gap and potential applications in flexible optoelectronic devices.

Except for the most studied $Ti_3C_2T_x$ MXene, metallic Mo_2CT_x MXenes (Fig. 7g) have demonstrated applications in plasmonic photodetection operated in the 400–800 nm visible spectral range by Alshareef and co-workers.[55] Fig. 7h shows the *I*–*V* curves of the Mo_2CT_x thin film photodetector under dark and 660 nm Vis illumination with a bias voltage of ±1 V. The best performing device enabled by Mo_2CT_x nanoflakes delivered a photoresponsivity of 9 A W^{-1} and a specific detectivity of cti[11] Jones under 660 nm laser illumination. The excellent features of the Mo_2CT_x were further verified by electron energy loss spectroscopy (EELS) (Fig. 7i). As can be seen, neither the longitudinal plasmon modes (0.3 and 0.39 eV) nor the transversal mode (2.45 eV) covers the incident light sources (325 and 1064 nm), opening a new gate for MXenes in optical electronics.

4.2 Transistors

4.2.1 Conductive electrodes. Recently, considerable efforts have been dedicated to developing the potential application of MXene electrodes in electronics.[31,94] Representatively, Alshareef's

group[31] demonstrated that metallic $Ti_3C_2T_x$ MXene can be used as a gate, source, and drain electrode in the design of both n-type zinc oxide (ZnO) and p-type tin monoxide (SnO) thin film transistors (TFTs). The MXene solution with a concentration of 1.0–1.5 mg mL^{-1} was sprayed on a glass substrate to build the bottom ohmic conductive gate electrode. Next, the HfO_2 dielectric layer was deposited on the bottom MXene electrode. The n-type semiconducting ZnO/p-type SnO film was grown on top of HfO_2. Finally, the top MXene source/drain contact was patterned by the second spray-coating process. The complementary metal oxide semiconductor (CMOS) inverters with all-MXene contacts demonstrated the achieved good performances, proving the great application of MXene electrodes in TFT devices.

Large-scale production of conductive $Ti_3C_2T_x$ MXene electrode arrays at low cost holds great advantages over assembling flexible devices. Great efforts have been focused on promoting the development of MXene electrode arrays. For example, Cho and co-workers proposed a simple approach to prepare a large-area MXene electrode array on a flexible substrate.[95] Fig. 8a depicts the schematic images of organic field-effect transistor (OFET) arrays with $Ti_3C_2T_x$ MXene gate, source, and drain electrodes. The large size monolayer $Ti_3C_2T_x$ MXene flakes with a lateral size of 2.5 μm (Fig. 8b) were produced. In the detailed fabrication process, a poly (ethylene 2,6-naphthalate) (PEN) substrate was coated with 50 nm thick PVP to provide a uniform hydrophobic plane then treated with UV/ozone through a shadow mask to obtain a patterned hydrophilic surface, which was immersed in MXene aqueous solution to build the bottom electrode. A 500 nm thick PVP gate dielectric layer was then spin-coated onto the patterned MXene gate electrode substrate. Then a selective-wetting method was employed to prepare MXene source and drain electrodes. Finally, 40 nm thick p-type and n-type organic semiconductors were thermally evaporated on the channel region. The large-area uniformity of the 10 × 10 MXene electrode array patterned onto a 2 × 2 cm^2 substrate was suggested *via* mapping of the electrical conductivity, the average conductivity was 2.57 kS cm^{-1} and the standard deviation was 0.18 kS cm^{-1}. A digital image of the assembled MXene based OFETs is presented in Fig. 8c. The outstanding conductivity and high carrier mobility of ~1 cm^2 V^{-1} s^{-1} and an on–off current ratio of ~10^7 for both p-type and n-type OFETs suggest the potential of MXene materials in the OFET field.

Very recently, the $Ti_3C_2T_x$ MXene electrode has also been successfully applied in the fabrication of organic vertical photoelectric transistors.[58] Fig. 8d displays the schematic image of MXene based photoelectric transistors, where $Ti_3C_2T_x$ MXene served as source electrodes of the OFET. The output curves of the MXene based photoelectric transistors under small V_{DS} (voltage between the source and drain) are provided in Fig. 8e. From the curves, we can see the holes being injected from the Ohmic contact based Au–semiconductor interface, leading to a marginal modulation of I_{DS} (voltage between the source and drain) at different V_{GS} (voltage between the source and gate) values. When negative V_{DS} was applied, the hole injection from the Schottky barrier based MXene–semiconductor (Fig. 8f) interface, I_{DS} was efficiently modulated by V_{GS}. Moreover, the responsivity of the photoelectric transistors that can be modulated by the gate voltage shows the value of 366 A W^{-1}

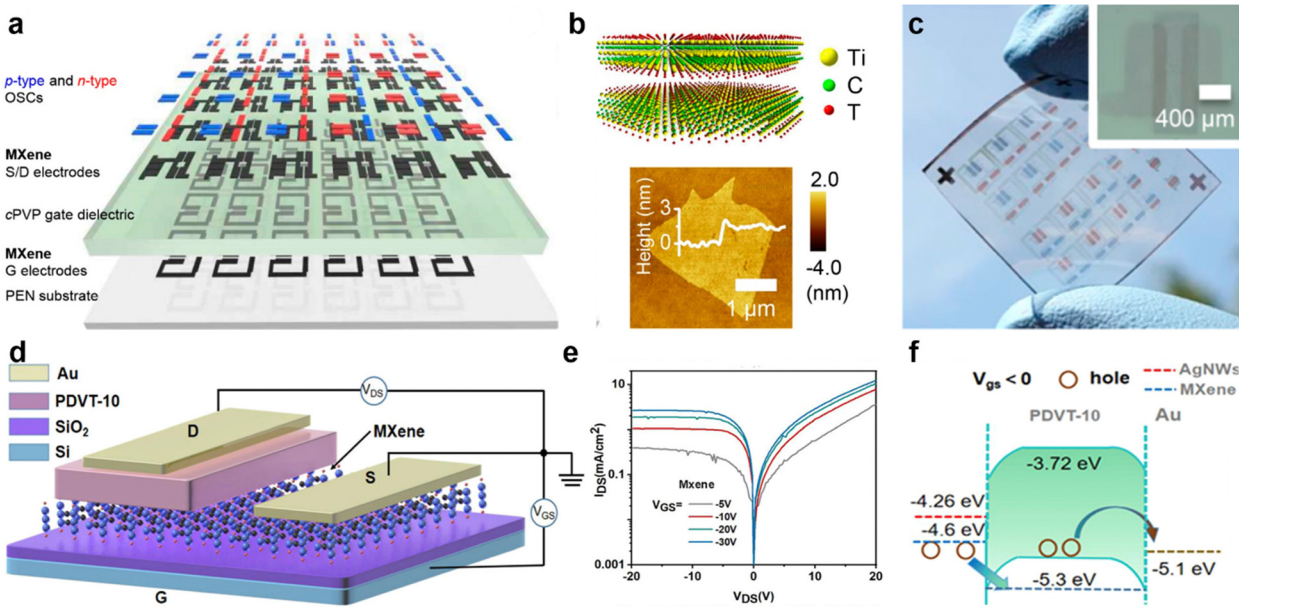

Fig. 8 Flexible transistors based on a $Ti_3C_2T_x$ electrode. All $Ti_3C_2T_x$ based OFET devices.[95] (a) Schematic images of the OFET devices. (b) Crystal structure and AFM image of the MXene flakes. (c) Photographic image of MXene-electrode-based OFETs. Reproduced with permission. Copyright 2019, American Chemical Society. MXene based photoelectric transistors.[58] (d) A schematic image of the MXene based photoelectric transistors. (e) Output curves of the MXene based photoelectric transistors under small V_{DS}. (f) Energy-band diagram of MXene based OFET. Reproduced with permission. Copyright 2022, Springer Nature.

under the weakest light intensity of 10 μW cm^{-2} at V_{GS} = −20 V. The photosensitivity reaches up to 7×10^4 under an illumination intensity of 500 μW cm^{-2} and the detectivity of the OFET is calculated to be 2.8×10^{12} Jones under a light intensity of 10 μW cm^{-2}. The outstanding performances demonstrate the wide application of the $Ti_3C_2T_x$ MXene electrode in FET devices.

4.2.2 Semiconductor layer. $Ti_3C_2T_x$ as a semiconductor layer in the fabrication of transistors was developed in 2023,[57] as shown in Fig. 9. Fig. 9a displays the schematic of the S-$Ti_3C_2T_x$ based transistor. The transistor transfer and output characteristic curves (Fig. 9b and c) demonstrate that the device has the function of gate voltage regulation, when positive V_G is applied, the I_{DS} decreases with the increase of the gate voltage. When the gate voltage is negative, more positive charges are induced at the interface of the oxide layer, and the source–drain current increases with the increase of the absolute value of the gate voltage, which conforms to the conductive behavior of the P-type S-$Ti_3C_2T_x$ semiconductor. By testing UPS and inverse photoemission spectroscopy (IPES), the work functions of S-$Ti_3C_2T_x$/$Ti_3C_2T_x$ MXene were 5.33 eV/4.45 eV by the tangent extrapolation method, the implantation barriers relative to the substrate and ionization potentials were 0.35 eV/0.03 eV, and 5.68 eV/4.48 eV, respectively, which determined the position of the Fermi level and material valence band (Fig. 9d and e). Combined with the measurement of the conduction band position by IPES, it can be concluded that the conduction band positions of S-$Ti_3C_2T_x$ and S-$Ti_3C_2T_x$ relative to the vacuum energy level were 4.38 eV and 4.75 eV, respectively (Fig. 9f and g). The successful manufacture of $Ti_3C_2T_x$ semiconductor layer based transistors paves the way for flexible multi-functional optoelectronic devices using all $Ti_3C_2T_x$ MXene materials. This work also inspires the creation of different kinds of MXene materials in flexible future electronic devices.

5. Application

5.1 Transparent electronics

Theoretic and experimental studies concerned with the optoelectronic performance of MXenes are constantly enriched in these years along with the development of optically transparent flexible electronics,[96] which will promote the development of optical communication, image recognition, artificial intelligence, *etc.*[97–102] Our group developed a transparent photodetector using Te microplates as photosensitive materials and $Ti_3C_2T_x$ as conductive electrodes.[103] Fig. 10a shows the structure of the transparent photodetector. The photoresponse comparison of the Te PDs with Ti_3C_2 and Au electrodes under dark current and 915 nm infrared light reveals that Ti_3C_2–Te PDs possess a higher on–off ratio, which is 13 times higher than that of Au–Te PDs owing to the strong van der Waals force between the Te microsheet and Ti_3C_2 nanoflakes. Fig. 10b displays the high transmittance of about 63% in the visible region, which suggests the excellent transparency of the assembled devices and could expand the application field of the Ti_3C_2–Te PDs. Moreover, the mechanical stability of the flexible Ti_3C_2–Te PDs (Fig. 10c) reveals the photocurrent and dark current of the flexible Ti_3C_2–Te PDs have no obvious change under increased bending angles varying from 0°, 30°, 60°, 90°, 120° to 150°.

Fang's group[59] synthesized a bionic transparent $Ti_3C_2T_x$ MXene thin film, which was used as the electrode of an ultraviolet

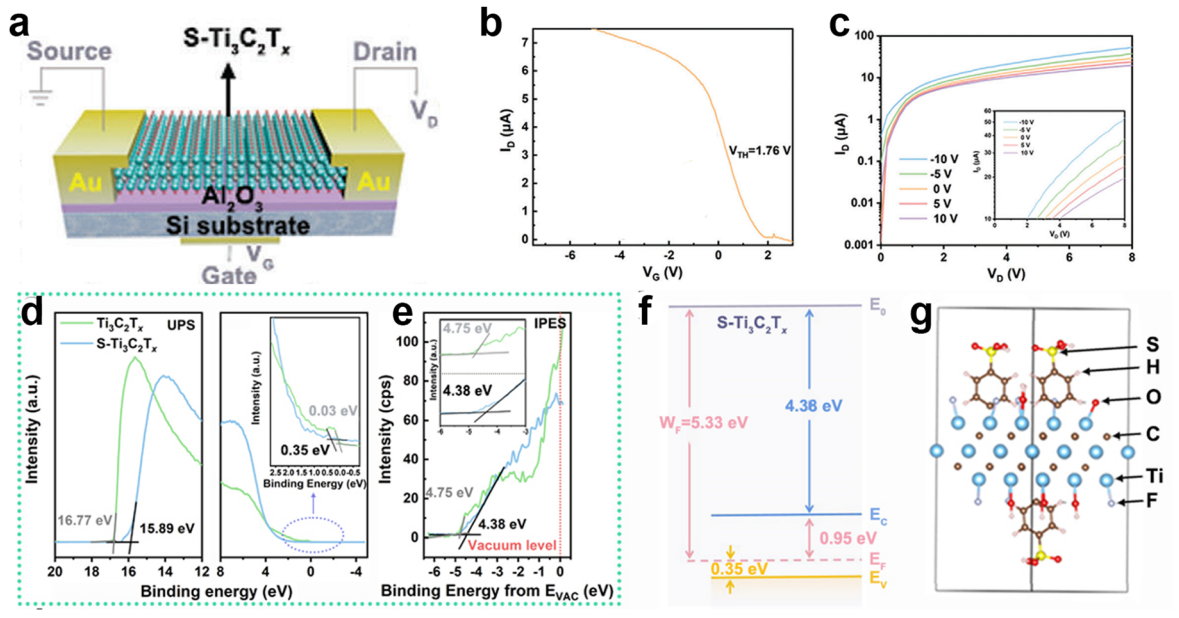

Fig. 9 Transistor using MXene as the semiconducting layer.[57] (a) Schematic diagram of the modified $Ti_3C_2T_x$ flakes (S-$Ti_3C_2T_x$). (b) Photographs of the fabricated S-$Ti_3C_2T_x$ devices under different bending states. (c) Multi-pixel points imaging based on S-$Ti_3C_2T_x$ photodetector arrays. (d, e) UPS and IPES curves of S-$Ti_3C_2T_x$ and $Ti_3C_2T_x$ MXene. (f, g) Schematic energy band and molecular model of S-$Ti_3C_2T_x$. Reproduced with permission. Copyright 2023, Wiley-VCH.

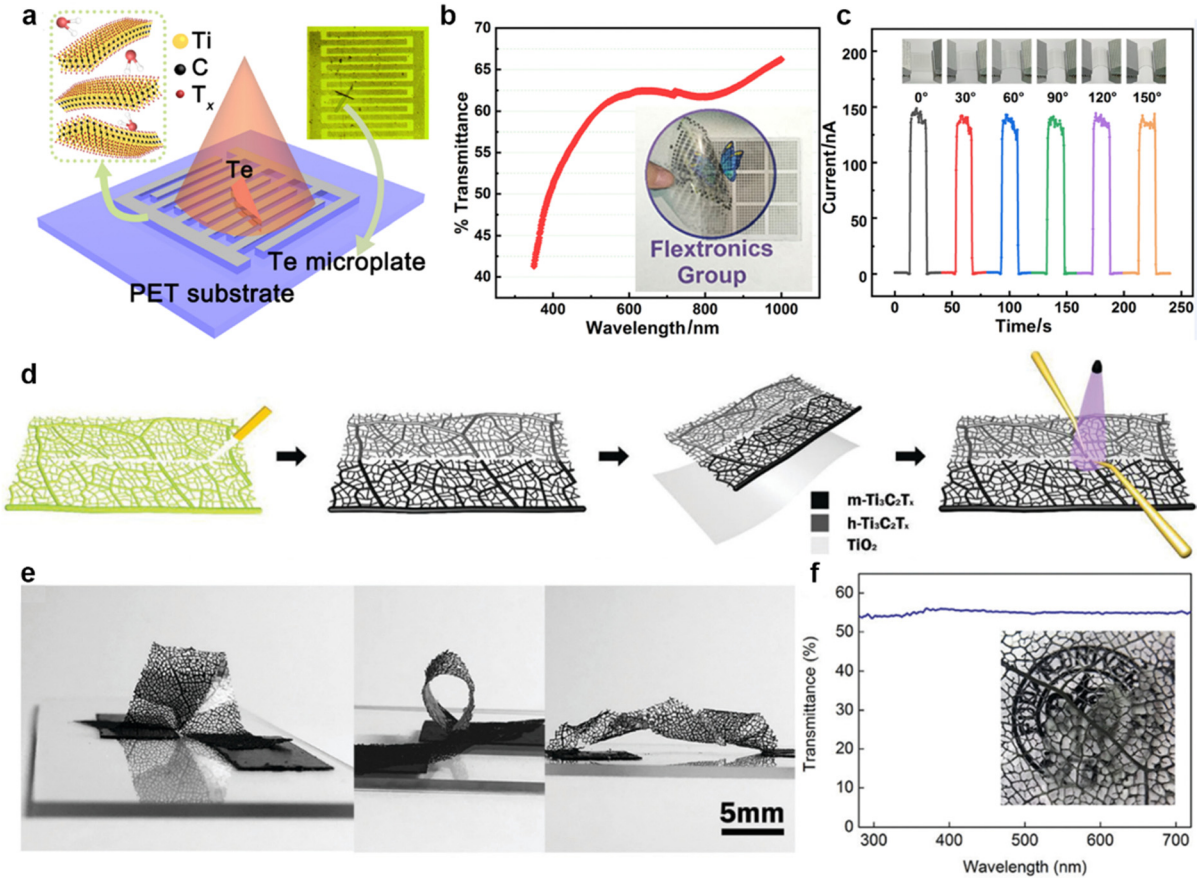

Fig. 10 MXene based transparent photodetector. (a) Schematic illustration and microphotography of the Ti_3C_2–Te–Ti_3C_2. (b) The transmittance of the assembled devices. (c) *I*–*T* curves of the prepared photodetector under the different bending states.[103] Reproduced with permission. Copyright 2021, Wiley-VCH. (d) Schematic illustration of the fabricating process of the transparent photodetector. (e) Digital photography of the devices. (f) The transmittance of the assembled devices.[59] Reproduced with permission. Copyright 2020, Royal Society of Chemistry.

(UV) photodetector. Fig. 6d shows the schematic process for fabricating the flexible transparent UV photodetector. Specifically, the leaf veins were first etched in a hot alkali solution, then the veins were dried, and finally a conductive $Ti_3C_2T_x$ slurry was coated on the surface of the veins, which shows a high transmittance of 90%. The prepared transparent conductive $Ti_3C_2T_x$ electrode was then used for the assembly of the flexible UV photodetector. Before the MXene solvent evaporates, a thin layer of electrospun TiO_2 film is glued to two $Ti_3C_2T_x$ blade electrodes to form an independent flexible photodetector. The digital photos of the photodetector under deformation in Fig. 10e demonstrate the excellent mechanical stability of the fabricated devices. Fig. 10f reveals that the photodetector has a high transmittance of up to 60%, which proves the feasibility of the application of MXene conductive electrodes in transparent electronic devices and also provides the possibility for the assembly of MXene in multi-functional electronic devices.

5.2 Flexible artificial neural network

Artificial neuromorphic vision electric devices that mimic human visual recognition systems have attracted extensive attention due to the potential for smart biomimetic robots, retinal/optic nerve/visual function recovery for the blind, and visual impairment.[104–106] Artificial neuromorphic vision electric devices usually consist of an image sensor array and neuromorphic units, realizing the reception, transformation, and acceptance of light information.[107–109] To optimize the artificial neuromorphic vision network, an image sensor array constructed by multi-pixel photodetectors is used as the pre-processing system to achieve photoelectric conversion.[110–112] Our group[57] designed a flexible artificial neuromorphic vision system to realize the photoelectric signal conversion, image learning, training, and recognition, as shown in Fig. 11. Fig. 11a displays the schematic diagram of the human visual system.

Fig. 11b and c depict the overall process of the artificial neural network (ANN), the image pre-processing model converts optical signals into electrical signals at first, and then transmits them to the three-layer ANN to finish learning, training and finally image recognition. Three letters "M", "A" and "X" were collected to form a database. Fig. 11d demonstrates the photodetector with Au and $Ti_3C_2T_x$ electrode has a comparable contrast, after the three-layer neural network trains and recognizes images in two databases, the recognition rate of the photodetector based on the Au electrode can reach 0.993 after 210 training epochs, and the recognition rate of the photodetector based on the $Ti_3C_2T_x$ electrode is 0.991. Fig. 11e and f provide the recognition probability map of three letters based on the S-$Ti_3C_2T_x$ artificial neural

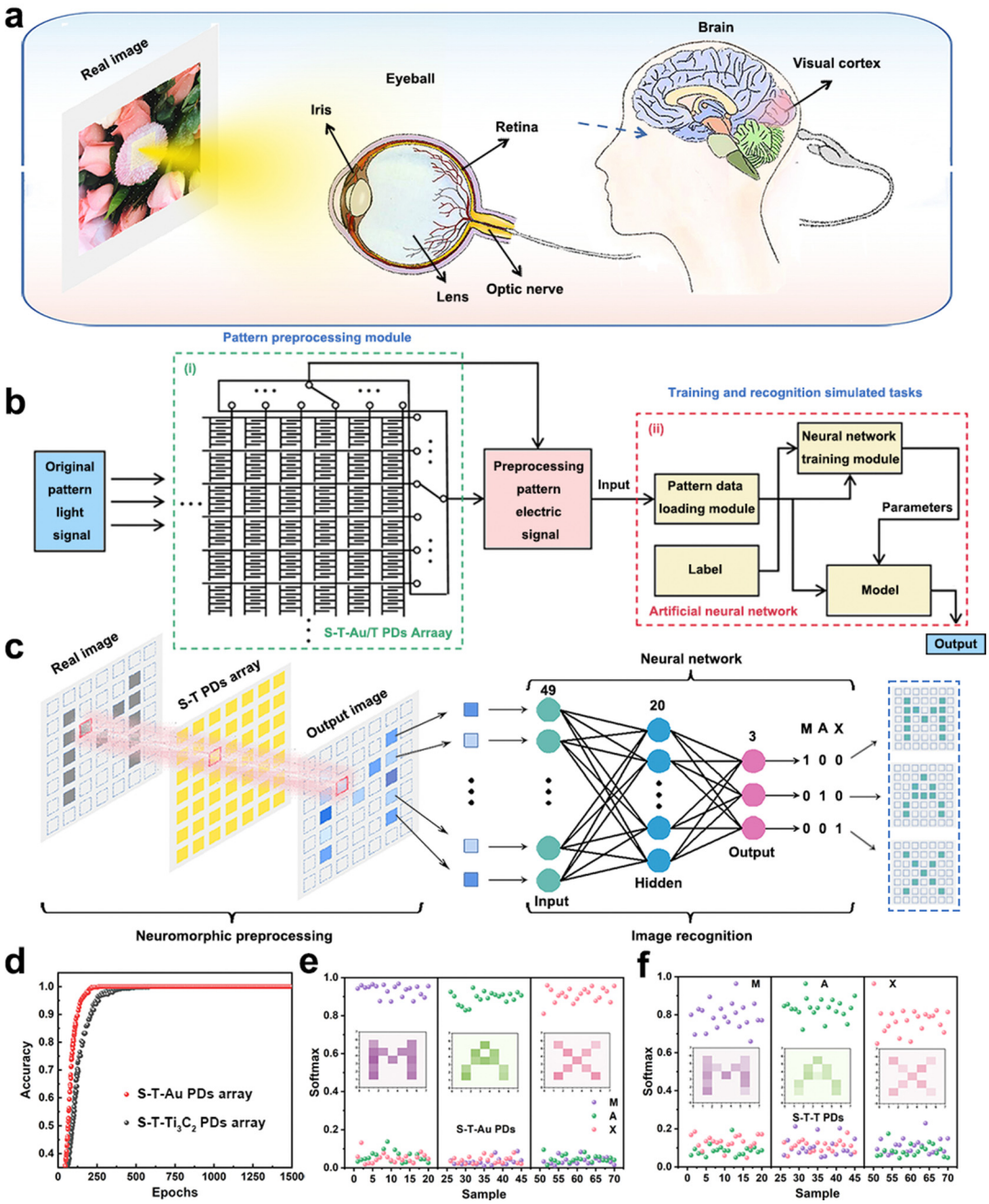

Fig. 11 Image recognition of the flexible artificial neural network (ANN).[57] (a) Schematic diagram of the human visual recognition system. (b) Flow chart of image training and recognition. (c) Schematic diagram of the ANN using photodetector array. (d) Comparison of recognition rate. (e) and (f) After learning a specific letter, the recognition probability map of three letters based on the S-$Ti_3C_2T_x$ artificial neural vision network with an Au electrode and $Ti_3C_2T_x$ electrode. Reproduced with permission. Copyright 2023, Wiley-VCH.

vision network with the Au electrode and $Ti_3C_2T_x$ electrode after learning a specific letter, and both kinds of devices can meet the image recognition requirements, demonstrating all-MXene materials based flexible integrated electronics.

6. Challenges and perspectives

In this review, the recent progress in MXene based flexible photodetectors is systematically summarized. We first discuss the metallic and semiconductor properties of MXene materials and then introduce the approaches used in fabricating MXene based flexible photodetectors, including photolithography, laser direct writing, spray coating, vacuum assisted filtration techniques. The heterojunctions and pure MXene based flexible photodetector along with their properties are also concluded. Moreover, the transistor with an MXene electrode or MXene semiconductor layer is presented. Despite the current research achievements on the fabrication of flexible

photodetectors with MXene materials, there are still many challenges. With the emergence of different synthesis methods of MXene materials, the continuous maturity of device processing technology, as well as the continuous in-depth exploration of the electrical and semiconductor properties of MXene materials, MXene materials will play an increasingly important role in the preparation of optoelectronic devices.

To further improve the optoelectronic performance of the MXene based flexible photodetector, the following research aspects should be seriously considered:

(1) The research on MXene materials in the field of optoelectronic devices is mainly on $Ti_3C_2T_x$ MXene, and most of the studies only focus on the high conductivity of MXene materials, and their semiconductor properties are less explored. More than 40 kinds of MXene materials have been synthesized, and their application in semiconductor devices is of importance to expand the MXene electronic devices.

(2) Single MXene flake based flexible photodetectors need to be designed to investigate the intrinsic electrical properties, which requires the preparation of large-size (>15 μm) MXene nanosheets and transfer methods to construct the photodetector devices or heterojunction. The heterojunction with single MXene flakes could also accelerate the development of MXene electronics.

(3) The emerging analysis like *in situ* TEM, *in situ* XRD, spectroscopy, *etc.* should be widely used to explore the semiconductor properties of MXene materials. Besides qualitative analysis of the terminals on the surface of Mxene materials, quantitative analysis also needs to be adopted to understand the properties of Mxene materials.

(4) Although DFT theoretical calculation shows that Sc_2C, Ti_2C, Zr_2C, Hf_2C, *etc.*, could deliver semiconductor properties, they are not applied in semiconductor devices. More attention should be paid to using Sc_2C, Ti_2C, Zr_2C, Hf_2C, *etc.* as photoresponse materials in the fabrication of flexible photodetectors or as a semiconductor layer in transistors.

(5) Stretchable or deformable photodetectors are the development trend of future optoelectronic devices. How to achieve these devices with high stability under stress through structural design of MXene materials at the micron scale or preparation of MXene films in wavy shape is also one of the important factors that needs to be considered.

(6) New fabrication technologies in MXene based optoelectronic devices should be developed to achieve the multi-pixel image sensor, thus expanding the application fields of flexible MXene electronic devices.

Author contributions

L. L. wrote the original draft. G. S. edited the article and provided the funding support.

Conflicts of interest

The authors declare no conflicts of interest.

Acknowledgements

This work was supported by the National Natural Science Foundation of China (61888102, 62004187, 52273256) and the Beijing Institute of Technology Research Found Program for Young Scholars.

Notes and references

1 B. Anasori, M. R. Lukatskaya and Y. Gogotsi, *Nat. Rev. Mater.*, 2017, **2**, 1–17.
2 B. Shi, L. Chen, T.-C. Jen, X. Liu, L. Li, A. Chen and G. Shen, *ACS Appl. Nano Mater.*, 2022, **6**, 315–322.
3 B. Shi, L. Li, A. Chen, T. C. Jen, X. Liu and G. Shen, *Nanomicro Lett.*, 2021, **14**, 1–10.
4 X. Xiao, H. Wang, P. Urbankowski and Y. Gogotsi, *Chem. Soc. Rev.*, 2018, **47**, 8744–8765.
5 A. Levitt, D. Hegh, P. Phillips, S. Uzun, M. Anayee, J. M. Razal, Y. Gogotsi and G. Dion, *Mater. Today*, 2020, **34**, 17–29.
6 H. Li, X. Chen, E. Zalnezhad, K. N. Hui, K. S. Hui and M. J. Ko, *J. Ind. Eng. Chem.*, 2020, **82**, 309–316.
7 L. Li, D. Chen and G. Shen, *Chem. Res. Chin. Univ.*, 2020, **36**, 694–698.
8 Y. Sun and W. G. Chong, *Mater. Horiz.*, 2023, **10**, 2373–2397.
9 Y. Wen, T. E. Rufford, X. Chen, N. Li, M. Lyu, L. Dai and L. Wang, *Nano Energy*, 2017, **38**, 368–376.
10 L. Li, X. Fu, S. Chen, S. Uzun, A. S. Levitt, C. E. Shuck, W. Han and Y. Gogotsi, *ACS Appl. Mater. Interfaces*, 2020, **12**, 15362–15369.
11 Q. Zhao, W. Zhou, M. Zhang, Y. Wang, Z. Duan, C. Tan, B. Liu, F. Ouyang, Z. Yuan, H. Tai and Y. Jiang, *Adv. Funct. Mater.*, 2022, **32**, 2270220.
12 Q. Zhao, Y. Jiang, L. Yuan, Z. Yuan, B. Zhang, B. Liu, M. Zhang, Q. Huang, Z. Duan and H. Tai, *Sens. Actuators, B*, 2023, **392**, 134082.
13 Q. Zhao, Y. Jiang, Z. Duan, Z. Yuan, J. Zha, Z. Wu, Q. Huang, Z. Zhou, H. Li, F. He, Y. Su, C. Tan and H. Tai, *Chem. Eng. J.*, 2022, **438**, 135588.
14 Q. Zhao, D. Sun, S. Wang, Z. Duan, Z. Yuan, G. Wei, J. L. Xu, H. Tai and Y. Jiang, *ACS Sens.*, 2021, **6**, 2858–2867.
15 Q.-N. Zhao, Y.-J. Zhang, Z.-H. Duan, S. Wang, C. Liu, Y.-D. Jiang and H.-L. Tai, *Rare Met.*, 2020, **40**, 1459–1476.
16 S. Wang, B. Liu, Z. Duan, Q. Zhao, Y. Zhang, G. Xie, Y. Jiang, S. Li and H. Tai, *Sens. Actuators, B*, 2021, **327**, 128923.
17 R. A. Soomro, S. Jawaid, Q. Zhu, Z. Abbas and B. Xu, *Chin. Chem. Lett.*, 2020, **31**, 922–930.
18 K. AlHassoon, M. Han, Y. Malallah, V. Ananthakrishnan, R. Rakhmanov, W. Reil, Y. Gogotsi and A. S. Daryoush, *Appl. Phys. Lett.*, 2020, **116**, 184101.
19 F. Shahzad, M. Alhabeb, C. B. Hatter, B. Anasori, S. Man Hong, C. M. Koo and Y. Gogotsi, *Science*, 2016, **353**, 1137–1140.
20 R. Sun, H.-B. Zhang, J. Liu, X. Xie, R. Yang, Y. Li, S. Hong and Z.-Z. Yu, *Adv. Funct. Mater.*, 2017, **27**, 1702807.

21 L. Li, C. Hu and G. Shen, *Acc. Mater. Res.*, 2021, **2**, 954–965.
22 M. Mariano, O. Mashtalir, F. Q. Antonio, W. H. Ryu, B. C. Deng, F. N. Xia, Y. Gogotsi and A. D. Taylor, *Nanoscale*, 2016, **8**, 16371–16378.
23 A. Djire, H. Y. Zhang, J. Liu, E. M. Miller and N. R. Neale, *ACS Appl. Mater. Interfaces*, 2019, **11**, 11812–11823.
24 Z. Du, W. Liu, J. Liu, Z. Chu, F. Qu, L. Li and G. Shen, *Adv. Mater. Interfaces*, 2023, 2300266.
25 C. E. Shuck, A. Sarycheva, M. Anayee, A. Levitt, Y. Z. Zhu, S. Uzun, V. Balitskiy, V. Zahorodna, O. Gogotsi and Y. Gogotsi, *Adv. Eng. Mater.*, 2020, **22**, 125786.
26 V. M. Hong, Ng, H. Huang, K. Zhou, P. S. Lee, W. Que, J. Z. Xu and L. B. Kong, *J. Mater. Chem. A*, 2017, **5**, 3039–3068.
27 K. Huang, Z. Li, J. Lin, G. Han and P. Huang, *Chem. Soc. Rev.*, 2018, **47**, 5109–5124.
28 P. Srimuk, F. Kaasik, B. Krüner, A. Tolosa, S. Fleischmann, N. Jäckel, M. C. Tekeli, M. Aslan, M. E. Suss and V. Presser, *J. Mater. Chem. A*, 2016, **4**, 18265–18271.
29 X. Chen, Z. Shi, Y. Tian, P. Lin, D. Wu, X. Li, B. Dong, W. Xu and X. Fang, *Mater. Horiz.*, 2021, **8**, 2929–2963.
30 K. A. S. Usman, S. Qin, L. C. Henderson, J. Zhang, D. Y. Hegh and J. M. Razal, *Mater. Horiz.*, 2021, **8**, 2886–2912.
31 Z. Wang, H. Kim and H. N. Alshareef, *Adv. Mater.*, 2018, **30**, e1706656.
32 H. Xu, A. Ren, J. Wu and Z. Wang, *Adv. Funct. Mater.*, 2020, 2000907.
33 X. Xu, T. Guo, M. Lanza and H. N. Alshareef, *Matter*, 2023, **6**, 800–837.
34 X. Cai, Y. Luo, B. Liu and H. M. Cheng, *Chem. Soc. Rev.*, 2018, **47**, 6224–6266.
35 H. Li, Z. Dong, Y. Zhang, L. Li, Z. Wang, C. Wang, K. Zhang and H. Zhang, *2D Mater.*, 2020, **8**, 012001.
36 P. Wang, S. Liu, W. Luo, H. Fang, F. Gong, N. Guo, Z. G. Chen, J. Zou, Y. Huang, X. Zhou, J. Wang, X. Chen, W. Lu, F. Xiu and W. Hu, *Adv. Mater.*, 2017, **29**, 1604439.
37 Z. Wang, W. Zhu, Y. Qiu, X. Yi, A. von dem Bussche, A. Kane, H. Gao, K. Koski and R. Hurt, *Chem. Soc. Rev.*, 2016, **45**, 1750–1780.
38 J. Xu, J. Shim, J. H. Park and S. Lee, *Adv. Funct. Mater.*, 2016, **26**, 5328–5334.
39 M. Alhabeb, K. Maleski, B. Anasori, P. Lelyukh, L. Clark, S. Sin and Y. Gogotsi, *Chem. Mater.*, 2017, **29**, 7633–7644.
40 A. Shayesteh Zeraati, S. A. Mirkhani, P. Sun, M. Naguib, P. V. Braun and U. Sundararaj, *Nanoscale*, 2021, **13**, 3572–3580.
41 H. Zhang, G. Yang, X. Zuo, H. Tang, Q. Yang and G. Li, *J. Mater. Chem. A*, 2016, **4**, 12913–12920.
42 K. Hantanasirisakul and Y. Gogotsi, *Adv. Mater.*, 2018, **30**, e1804779.
43 T. S. Mathis, K. Maleski, A. Goad, A. Sarycheva, M. Anayee, A. C. Foucher, K. Hantanasirisakul, C. E. Shuck, E. A. Stach and Y. Gogotsi, *ACS Nano*, 2021, **15**, 6420–6429.
44 M. Q. Zhao, X. Xie, C. E. Ren, T. Makaryan, B. Anasori, G. Wang and Y. Gogotsi, *Adv. Mater.*, 2017, **29**, 1702410.
45 J. Zhu, E. Ha, G. Zhao, Y. Zhou, D. Huang, G. Yue, L. Hu, N. Sun, Y. Wang, L. Y. S. Lee, C. Xu, K.-Y. Wong, D. Astruc and P. Zhao, *Coordin. Chem. Rev.*, 2017, **352**, 306–327.
46 L. Gao, Y. Zhao, X. Chang, J. Zhang, Y. Li, S. Wageh, O. A. Al-Hartomy, A. G. Al-Sehemi, H. Zhang and H. Ågren, *Mater. Today*, 2022, **61**, 169–190.
47 S. Ali, A. Raza, A. M. Afzal, M. W. Iqbal, M. Hussain, M. Imran and M. A. Assiri, *Adv. Mater. Interfaces*, 2022, **9**, 2200556.
48 A. Sreedhar, Q. T. H. Ta and J.-S. Noh, *J. Ind. Eng. Chem.*, 2023, **127**, 1–17.
49 B. Wang, S. Zhong, P. Xu and H. Zhang, *Chem. Eng. J.*, 2021, **403**, 126336.
50 M. Ghidiu, M. R. Lukatskaya, M. Q. Zhao, Y. Gogotsi and M. W. Barsoum, *Nature*, 2014, **516**, 78–81.
51 C. Hu, Z. Du, Z. Wei, L. Li and G. Shen, *Appl. Phys. Rev.*, 2023, **10**, 021402.
52 C. Hu, H. Chen, L. Li, H. Huang and G. Shen, *Adv. Mater. Technol.*, 2022, **7**, 2101639.
53 L. Li, W. Liu, K. Jiang, D. Chen, F. Qu and G. Shen, *Nanomicro Lett.*, 2021, **13**, 100.
54 W. Liu, L. Li and G. Shen, *Nanoscale*, 2023, **15**, 2624–2632.
55 D. B. Velusamy, J. K. El-Demellawi, A. M. El-Zohry, A. Giugni, S. Lopatin, M. N. Hedhili, A. E. Mansour, E. D. Fabrizio, O. F. Mohammed and H. N. Alshareef, *Adv. Mater.*, 2019, **31**, e1807658.
56 B. Li, Q. B. Zhu, C. Cui, C. Liu, Z. H. Wang, S. Feng, Y. Sun, H. L. Zhu, X. Su, Y. M. Zhao, H. W. Zhang, J. Yao, S. Qiu, Q. W. Li, X. M. Wang, X. H. Wang, H. M. Cheng and D. M. Sun, *Adv. Mater.*, 2022, **34**, e2201298.
57 C. Hu, Z. Wei, L. Li and G. Shen, *Adv. Funct. Mater.*, 2023, 2302188.
58 E. Li, C. Gao, R. Yu, X. Wang, L. He, Y. Hu, H. Chen, H. Chen and T. Guo, *Nat. Commun.*, 2022, **13**, 2898.
59 J. Chen, Z. Li, F. Ni, W. Ouyang and X. Fang, *Mater. Horiz.*, 2020, **7**, 1828–1833.
60 A. Sinha, Dhanjai, H. Zhao, Y. Huang, X. Lu, J. Chen and R. Jain, *TrAC, Trends Anal. Chem.*, 2018, **105**, 424–435.
61 C. Yang, Y. Tang, Y. Tian, Y. Luo, M. Faraz Ud Din, X. Yin and W. Que, *Adv. Energy Mater.*, 2018, **8**, 1802087.
62 C. J. Zhang, B. Anasori, A. Seral-Ascaso, S. H. Park, N. McEvoy, A. Shmeliov, G. S. Duesberg, J. N. Coleman, Y. Gogotsi and V. Nicolosi, *Adv. Mater.*, 2017, **29**, 1706278.
63 J. Zhang, N. Kong, S. Uzun, A. Levitt, S. Seyedin, P. A. Lynch, S. Qin, M. Han, W. Yang, J. Liu, X. Wang, Y. Gogotsi and J. M. Razal, *Adv. Mater.*, 2020, **32**, e2001093.
64 H. Qing, W. Chenxu, Z. Shuang, H. A. N. Meikang, S. U. N. Zhengming, Z. Peigen, H. Zhenying, Z. Yiming, W. Junjie, S. U. N. Zhimei, Z. Bikun, B. A. I. Yuelei, Y. I. N. Hang, J. Rosen, T. A. O. Quanzheng, Z. Jie, X. Yukun, C. Ke, L. I. Youbing, L. I. Mian and D. Haoming, *J. Inorg. Mater.*, 2023, **38**, 845–884.
65 M. Sokol, V. Natu, S. Kota and M. W. Barsoum, *Trend. Chem.*, 2019, **1**, 210–223.
66 W. Liu, L. Li, C. Hu, D. Chen and G. Shen, *Adv. Mater. Technol.*, 2022, **7**, 2200158.
67 Y. Y. Liu, H. Xiao and W. A. Goddard, *J. Am. Chem. Soc.*, 2016, **138**, 15853–15856.
68 T. Schultz, N. C. Frey, K. Hantanasirisakul, S. Park, S. J. May, V. B. Shenoy, Y. Gogotsi and N. Koch, *Chem. Mater.*, 2019, **31**, 6590–6597.

69 J. L. Hart, K. Hantanasirisakul, A. C. Lang, B. Anasori, D. Pinto, Y. Pivak, J. T. van Omme, S. J. May, Y. Gogotsi and M. L. Taheri, *Nat. Commun.*, 2019, **10**, 522.
70 L. Li, Z. Lou and G. Shen, *Adv. Funct. Mater.*, 2018, **28**, 1705389.
71 W. Ran, L. Wang, S. Zhao, D. Wang, R. Yin, Z. Lou and G. Shen, *Adv. Mater.*, 2020, **32**, e1908419.
72 Z. Duan, C. Hu, W. Liu, J. Liu, Z. Chu, W. Yang, L. Li and G. Shen, *Adv. Mater. Technol.*, 2023, 2300157.
73 L. Q. Tao, H. Tian, Y. Liu, Z. Y. Ju, Y. Pang, Y. Q. Chen, D. Y. Wang, X. G. Tian, J. C. Yan, N. Q. Deng, Y. Yang and T. L. Ren, *Nat. Commun.*, 2017, **8**, 14579.
74 X. Xu, L. Li, W. Liu, Z. Chen, D. Chen and G. Shen, *Adv. Mater. Interfaces*, 2022, **9**, 2201165.
75 L. Li, S. Ye, J. Qu, F. Zhou, J. Song and G. Shen, *Small*, 2021, **17**, e2005606.
76 L. D. Li, L. L. Gu, Z. Lou, Z. Y. Fan and G. Z. Shen, *ACS Nano*, 2017, **11**, 4067–4076.
77 L. Lv, W. Dang, X. X. Wu, H. Chen, T. Wang, L. Q. Qin, Z. X. Wei, K. Zhang, G. Z. Shen and H. Huang, *Macromolecules*, 2020, **53**, 10636–10643.
78 Y. Wang, J. Kublitski, S. Xing, F. Dollinger, D. Spoltore, J. Benduhn and K. Leo, *Mater. Horiz.*, 2022, **9**, 220–251.
79 J. Yoon, G.-Y. Bae, S. Yoo, J. I. Yoo, N.-H. You, W.-K. Hong and H. C. Ko, *J. Alloys Compd.*, 2020, **817**, 152788.
80 K. Montazeri, M. Currie, L. Verger, P. Dianat, M. W. Barsoum and B. Nabet, *Adv. Mater.*, 2019, **31**, e1903271.
81 D. Dumcenco, D. Ovchinnikov, K. Marinov, P. Lazic, M. Gibertini, N. Marzari, O. Lopez Sanchez, Y. C. Kung, D. Krasnozhon, M. W. Chen, S. Bertolazzi, P. Gillet, A. Fontcuberta i Morral, A. Radenovic and A. Kis, *ACS Nano*, 2015, **9**, 4611–4620.
82 F. Huang, J. Li, Z. Xu, Y. Liu, R. Luo, S. W. Zhang, P. Nie, Y. Lv, S. Zhao, W. Su, W. D. Li, S. Zhao, G. Wei, H. C. Kuo and F. Kang, *Nanomaterials*, 2019, **9**, 1312.
83 K. Thakar, B. Mukherjee, S. Grover, N. Kaushik, M. Deshmukh and S. Lodha, *ACS Appl. Mater. Interfaces*, 2018, **10**, 36512–36522.
84 A. Wadsworth, Z. Hamid, J. Kosco, N. Gasparini and I. McCulloch, *Adv. Mater.*, 2020, **32**, e2001763.
85 Y. T. Liu, P. Zhang, N. Sun, B. Anasori, Q. Z. Zhu, H. Liu, Y. Gogotsi and B. Xu, *Adv. Mater.*, 2018, **30**, e1707334.
86 S. Chertopalov and V. N. Mochalin, *ACS Nano*, 2018, **12**, 6109–6116.
87 W. Deng, H. Huang, H. Jin, W. Li, X. Chu, D. Xiong, W. Yan, F. Chun, M. Xie, C. Luo, L. Jin, C. Liu, H. Zhang, W. Deng and W. Yang, *Adv. Opt. Mater.*, 2019, **7**, 1801521.
88 W. Song, J. Chen, Z. Li and X. Fang, *Adv. Mater.*, 2021, **33**, e2101059.
89 J. J. Tao, J. Jiang, S. N. Zhao, Y. Zhang, X. X. Li, X. Fang, P. Wang, W. Hu, Y. H. Lee, H. L. Lu and D. W. Zhang, *ACS Nano*, 2021, **15**, 3241–3250.
90 W. Ouyang, J. Chen, J. H. He and X. Fang, *Adv. Electron. Mater.*, 2020, **6**, 2000168.
91 Z. Kang, Y. Ma, X. Tan, M. Zhu, Z. Zheng, N. Liu, L. Li, Z. Zou, X. Jiang, T. Zhai and Y. Gao, *Adv. Electron. Mater.*, 2017, **3**, 1700165.
92 J. Jeon, H. Choi, S. Choi, J. H. Park, B. H. Lee, E. Hwang and S. Lee, *Adv. Funct. Mater.*, 2019, **29**, 1905384.
93 X. Jiang, S. Liu, W. Liang, S. Luo, Z. He, Y. Ge, H. Wang, R. Cao, F. Zhang, Q. Wen, J. Li, Q. Bao, D. Fan and H. Zhang, *Laser Photonics Rev.*, 2018, **12**, 1700229.
94 B. Xu, M. Zhu, W. Zhang, X. Zhen, Z. Pei, Q. Xue, C. Zhi and P. Shi, *Adv. Mater.*, 2016, **28**, 3333–3339.
95 B. Lyu, M. Kim, H. Jing, J. Kang, C. Qian, S. Lee and J. H. Cho, *ACS Nano*, 2019, **13**, 11392–11400.
96 J. Liu, L. Zhang and C. Z. Li, *Ind. Eng. Chem. Res.*, 2019, **58**, 21485–21492.
97 M. Hossain, G. S. Kumar, S. N. B. Prabhava, E. D. Sheerin, D. McCloskey, S. Acharya, K. D. M. Rao and J. J. Boland, *ACS Nano*, 2018, **12**, 4727–4735.
98 Q. Li, J. van de Groep, Y. Wang, P. G. Kik and M. L. Brongersma, *Nat. Commun.*, 2019, **10**, 4982.
99 M.-B. Lien, C.-H. Liu, I. Y. Chun, S. Ravishankar, H. Nien, M. Zhou, J. A. Fessler, Z. Zhong and T. B. Norris, *Nat. Photonics*, 2020, **14**, 143–148.
100 C. Wang, D. Hwang, Z. Yu, K. Takei, J. Park, T. Chen, B. Ma and A. Javey, *Nat. Mater.*, 2013, **12**, 899–904.
101 Q. Wang, M. Jian, C. Wang and Y. Zhang, *Adv. Funct. Mater.*, 2017, **27**, 1605657.
102 R. X. Xu, L. L. Min, Z. M. Qi, X. Y. Zhang, J. Jian, Y. D. Ji, F. J. Qian, J. Y. Fan, C. X. Kan, H. Y. Wang, W. Tian, L. Li, W. W. Li and H. Yang, *ACS Appl. Mater. Interfaces*, 2020, **12**, 16462–16468.
103 C. Hu, L. Li and G. Shen, *Chin. J. Chem.*, 2021, **39**, 2141–2146.
104 S. Chen, Z. Lou, D. Chen and G. Shen, *Adv. Mater.*, 2018, **30**, 1705400.
105 S. H. Kim, G. W. Baek, J. Yoon, S. Seo, J. Park, D. Hahm, J. H. Chang, D. Seong, H. Seo, S. Oh, K. Kim, H. Jung, Y. Oh, H. W. Baac, B. Alimkhanuly, W. K. Bae, S. Lee, M. Lee, J. Kwak, J. H. Park and D. Son, *Adv. Mater.*, 2021, **33**, e2104690.
106 J. Tang, F. Yuan, X. Shen, Z. Wang, M. Rao, Y. He, Y. Sun, X. Li, W. Zhang, Y. Li, B. Gao, H. Qian, G. Bi, S. Song, J. J. Yang and H. Wu, *Adv. Mater.*, 2019, **31**, e1902761.
107 J. Du, D. Xie, Q. Zhang, H. Zhong, F. Meng, X. Fu, Q. Sun, H. Ni, T. Li, E.-J. Guo, H. Guo, M. He, C. Wang, L. Gu, X. Xu, G. Zhang, G. Yang, K. Jin and C. Ge, *Nano Energy*, 2021, **89**, 106439.
108 Z. Y. Hu, Y. L. Zhang, C. Pan, J. Y. Dou, Z. Z. Li, Z. N. Tian, J. W. Mao, Q. D. Chen and H. B. Sun, *Nat. Commun.*, 2022, **13**, 5634.
109 Q. B. Zhu, B. Li, D. D. Yang, C. Liu, S. Feng, M. L. Chen, Y. Sun, Y. N. Tian, X. Su, X. M. Wang, S. Qiu, Q. W. Li, X. M. Li, H. B. Zeng, H. M. Cheng and D. M. Sun, *Nat. Commun.*, 2021, **12**, 1798.
110 L. Gu, S. Poddar, Y. Lin, Z. Long, D. Zhang, Q. Zhang, L. Shu, X. Qiu, M. Kam, A. Javey and Z. Fan, *Nature*, 2020, **581**, 278–282.
111 L. Gu, M. M. Tavakoli, D. Zhang, Q. Zhang, A. Waleed, Y. Xiao, K. H. Tsui, Y. Lin, L. Liao, J. Wang and Z. Fan, *Adv. Mater.*, 2016, **28**, 9713–9721.
112 S. Wang, X. Chen, X. Huang, D. Wei Zhang and P. Zhou, *Adv. Intelligent Systems*, 2020, **2**, 2000124.